Master's thesis

Probing the ^{16}O compound nucleus via ^{15}N(p,α)^{12}C reactions

Kenneth Lund Andersen

AARHUS
UNIVERSITY

Colophon

Probing the ^{16}O compound nucleus via $^{15}N(p,\alpha)^{12}C$ reactions

Probing the ^{16}O compound nucleus via ^{15}N(p,α)^{12}C reactions

Kenneth Lund Andersen

Master's thesis

September 2018

Supervisor: Hans Fynbo

Department of Physics and Astronomy

University of Aarhus

Abstract

This thesis presents measurement of the ^{16}O excitation function from proton energies of 300 to 3800 keV. This energy scan will provide information on the level structure of ^{16}O through the ^{15}N(p,α_x)^{12}C reactions. This includes cross sections, partial widths, spin parities and energies of the excited states. Cross sections will serve as input in future R-matrix analyses, providing the foundation for extrapolating the level structure of ^{16}O down to the relevant astrophysical energies. The scan will be aided by additional analysis of possible gamma transitions to unbound states in ^{16}O that subsequently alpha-decay into ^{12}C. These transitions have rarely been observed and never subsequently confirmed. A strong candidate for such an intermediate state is the 1^- state at an excitation energy of 9.59 MeV. This state is one of two strong contributors to the low-end cross section of the ^{12}C(α,γ)^{16}O reaction, which is of great importance to both hydrogen burning through the CNO-cycle and helium burning through the triple alpha process. Simulations of the possible four alpha breakup of ^{16}O is also investigated at proton energies from 3000 to 4000 keV, since a strong candidate for the four alpha cluster state is located within the range of the scan at an excitation energy of 15.10 MeV.

Measurements were carried out at the 5 MV Van de Graff accelerator facility at Aarhus University. Measurements were performed in two different experiments, the IFA022 and IFA028 experiments. IFA022 focuses on the low energy range of the scan, from 300 to 2000 keV and was carried out in October and November of 2017. IFA028 focuses on the higher energies from 2000 to 3800 keV and was carried out in March and April of 2018. Both experiments use a proton beam impacting on a ^{15}N target on a carbon backing.

The analysis was performed in ROOT, a C++ framework used by many nuclear physics experimentalists. AUSAlib, a framework of programs build to facilitate the analysis of experimental data, is used extensively throughout the analysis, and

chapter 3 is devoted entirely to explaining the process from unpacked data to analyzed data using the many features of AUSAlib.

The results of the energy scan is information on nine different states through the α_0 and α_1 reaction channels. A rough peak fitting routine utilizing the Breit-Wigner formalism has provided partial widths and energies of the excited states for each of these nine states. Several other states are observed, but not strongly enough to definitively provide widths and centroid energies. A more detailed fit using the sum of three peaks has been fitted to three states in the α_0 channel. This has led to a state previously proposed at a proton energy of 1050 ± 150 keV being observed at 1078 ± 4 keV. Angular distributions for every run has also been produced and are ready to be used as input for a more advanced analysis, such as an R-matrix fit. Such an analysis will produce more reliable information on every single state, as the Breit-Wigner formalism is meant only for describing isolated single peaks, meaning the method is inherently flawed when used in this context, and should only taken as a first approximation.

Contents

Chapter 1

Introduction

At first there was nothing – or any concept of nothingness for that matter, but then all of a sudden, the Big Bang. This apparent birth of the Universe happened 13.8 billion years ago [1] and the baryonic matter that is left from this great beginning takes the form of hydrogen, helium and very small amounts of heavier elements. Through many life cycles of massive stars exploding in violent supernovae, these leftovers from the Big Bang has been transformed into all elements known to man. This process is called nucleosynthesis, and the varying amounts of each element are called abundances. These abundances play an important role in how our Universe functions. Imagine life with no carbon or oxygen. Such a thing would be very different from the life we know.

The abundances that can be observed throughout the Universe are the products of tens of thousands of nuclear reactions, happening in the extreme conditions of a supernova or inside the core of a star. Even though many nuclei are involved in these reactions, only a small fraction really has a large impact on the resulting abundances. One such nucleus is ^{16}O. The level structure of ^{16}O strongly influences the CNO cycle and also characterizes the endpoint of stellar helium burning in a reaction which is dubbed the "Holy Grail" of nuclear astrophysics. This makes ^{16}O a very interesting nucleus to study, and various experiments have been devised to determine the workings of this particular nucleus.

1.1 Astrophysical Significance

In low mass main sequence stars the pp-process dominates the energy production, but in higher mass stars, M > 1.5$M_{\odot}$, the energy production is dominated by the CNO-cycle, a catalytic reaction sequence. The CNO-cycle combines four protons into one helium atom. A visual representation of the CNO-cycle can be seen in figure 1.1 with two sub-cycles and a branching point once 15N is obtained.

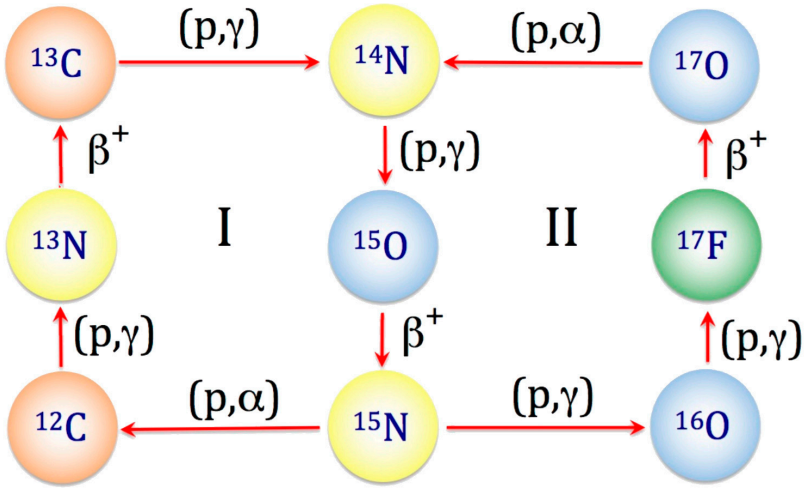

Figure 1.1: *The CNO-cycle. The level structure of the compound nucleus ^{16}O dictates whether the CNO I cycle starts over once it arrives at ^{15}N or continues into the CNO II cycle. The illustration is from [2].*

The cycle proceeds from ^{15}N with a proton capture followed by emission of either an alpha particle or a gamma ray. Thus the structure of the compound nucleus ^{16}O dictates the branching of ^{15}N(p,γ)^{16}O versus ^{15}N(p,α)^{12}C. This branching ratio has a large impact on stellar evolution, and substantial effort has been put into constraining it. Even with several attempts to constrain the cross section of this reaction at relevant energies, the needed constraining is not yet achieved. Three main physical contributers make this constraining difficult, the first being resonant contributions from two 1^- levels in ^{16}O at E_x = 12.45 and 13.09 MeV. The second is external radiative capture to the ground state, and the third is tails of higher energy resonances [3]. All of these contributions need to be well known, before they can be extrapolated to stellar energies. The desired level of uncertainty is $\sim 10\,\%$ [6].

When hydrogen in the core of the star is depleted, the core will contract due to the loss in outwards radiative pressure. Due to this contraction, temperatures in the core will start to rise. Once temperatures reach a certain level, the contraction will seize due to the ignition of helium burning. Helium burning is triggered by the triple-alpha process, where three alpha particles combine to form ^{12}C. The simultaneous fusion of three alpha particles is very unlikely even in stellar environments and a two step process, first fusing two alphas to ^{8}Be, is indeed much more efficient. However, the unstable nature of ^{8}Be, makes the second alpha capture a race for time. In 1954 Hoyle proposed a resonant state in ^{12}C that would enhance the cross section of the second capture and make the triple-alpha process much more likely [4].

After creating the stable ^{12}C, the process can be followed by a subsequent alpha capture which transforms ^{12}C into ^{16}O. Thus the abundances of ^{12}C and ^{16}O are determined by the competition between the triple-alpha process and the $^{12}C(\alpha,\gamma)^{16}O$ reaction, since they both need helium in order to complete the reaction. Once the helium is depleted, the ratio of carbon and oxygen is set.

Both of these reactions proceed through strong resonance mechanics, whereas the next alpha capture reaction $^{16}O(\alpha,\gamma)^{20}N$ lacks any such resonant enhancement, effectively preventing the star from burning helium further than ^{16}O. The abundances of ^{12}C and ^{16}O are therefore strongly dependent on the level structure of ^{16}O, since the $^{12}C(\alpha,\gamma)^{16}O$ reaction effectively controls the ratio of ^{12}C and ^{16}O. The ratio of these two elements is crucial to burning sequences at later stage stellar evolution, ignition mechanisms of thermonuclear supernovae [5] and in the end to the development of life here on earth.

1.2 Nuclear Physics

The temperatures at which stellar hydrogen burning occurs and to some extent also helium burning, corresponds to very low energy conditions in the lab. The cross section of the reactions are highly dependent on energy and decline as a function of that, due to the Coulomb barrier. This makes direct measurements of the reactions extremely challenging with existing technology, since the lower cross section combined with less energetic particles, demands high efficiency detectors and long running measurements or high beam currents. Presently, reactions are

carried out at higher energies, where cross sections are significantly higher. The cross sections are then extrapolated to lower energy ranges using techniques such as R-matrix analysis. These extrapolations to low energy stellar ranges only improves when more information about higher-energy features are added. This is yet another reason to study the level structure of nuclei at different energy ranges. A number of detailed R-matrix analyses regarding the ^{16}O nucleus with contributions from several different studies have been published by James deBoer in recent years [3], [6], and the work presented in this thesis, will likely become part of future R-matrix analyses.

As mentioned earlier, large amounts of experimental data have been accumulated in order to study the ^{16}O nucleus. This includes studies of the following reactions,

$$^{12}\mathrm{C}(\alpha,\alpha_0)^{12}\mathrm{C}, \quad ^{12}\mathrm{C}(\alpha,\alpha_1)^{12}\mathrm{C}, \quad ^{12}\mathrm{C}(\alpha,\mathrm{p})^{15}\mathrm{N}, \quad ^{12}\mathrm{C}(\alpha,\gamma)^{16}\mathrm{O},$$
$$^{15}\mathrm{N}(\mathrm{p},\mathrm{p})^{15}\mathrm{N}, \quad ^{15}\mathrm{N}(\mathrm{p},\alpha_0)^{12}\mathrm{C}, \quad ^{15}\mathrm{N}(\mathrm{p},\alpha_1)^{12}\mathrm{C}, \quad ^{15}\mathrm{N}(\mathrm{p},\gamma)^{16}\mathrm{O}.$$

The focus of this thesis will be on the ^{15}N(p,α_x)^{12}C reactions. The cross sections of these reactions are dominated by broad levels in the ^{16}O compound nucleus [7]. Populating these levels and observing the decay channels from them will provide great insights about the nucleus. In pursuit of a greater understanding of this, the upcoming sections will be dedicated to understanding the ^{15}N(p,α_x)^{12}C reactions and relating the properties of the outgoing particles to information about the ^{16}O nucleus.

The Reaction

As an example, let us consider the reaction between a stationary ^{15}N atom and a proton impacting it at a proton energy of 335 keV. This reaction populates the 1^- state in the resulting ^{16}O compound nucleus located at an excitation energy of 12.442 MeV, which subsequently decays into ^{12}C and an alpha particle. If this decay proceeds to the ground state of ^{12}C, the alpha particle will receive the maximum amount of kinetic energy. The alpha particles associated with this decay is denoted by α_0. If the decay instead proceeds to the first excited state in ^{12}C, located 4.43 MeV above the ground state, less energy will be available to the alpha particle. This alpha particle will be denoted by α_1. Populating subsequently higher states in ^{12}C will

in turn produce alpha particles with increasing subscripts. At a proton energy of 0.335 MeV, only the ground state and first excited state of ^{12}C can be populated.

By producing this reaction in a laboratory setting, we can attempt to detect the energies of the resulting particles and this we can infer information about the ^{16}O compound nucleus. From the number af detected particles versus number of ingoing particles, it is also possible to infer the cross section of the particular reaction, which then in turn also provides a lot of information about the compound nucleus.

The reaction outlined above could be drawn by connecting the different nuclei with arrows to show the reaction progressing in time, but it can also be illustrated in terms of a levels diagram. In figure 1.2 this can be seen with energies in MeV. This figure will be expanded upon in the upcoming sections as we explore the ^{16}O nucleus, until eventually it represents the entirety of the work presented in this thesis.

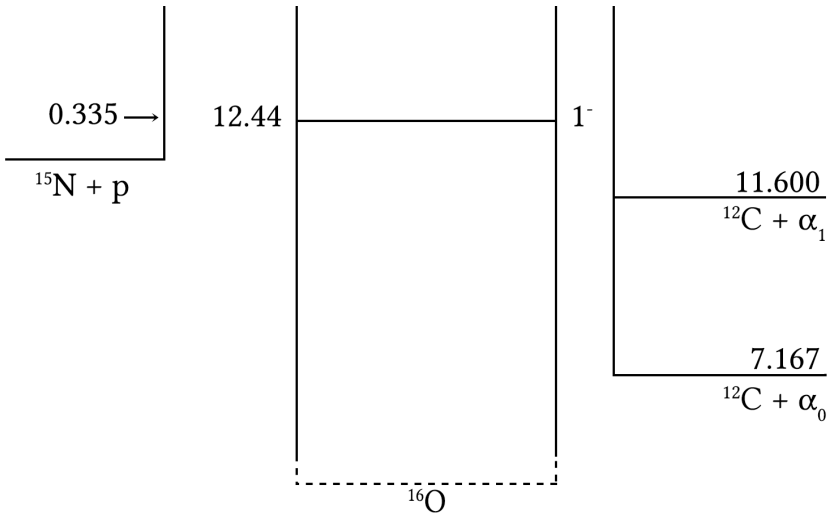

Figure 1.2: *A levels diagram describing the $^{15}N(p,\alpha_x)^{12}C$ reaction at an ingoing proton energy of* 0.335 MeV. *This figure will be expanded on to encapsulate the entire work presented in this thesis. Energies are in MeV.*

The Structure of ^{16}O

How the nucleons within the nucleus are distributed is not necessarily obvious. The liquid drop model and the Fermi gas model both predict nuclear properties to be smoothly varying as a function of number of nucleons. However, this should only

be taken as a description of the average trend. In the 1940s it became evident that nuclear properties have a tendency of discontinuous behavior and that this behavior happens at the same value for N and Z. These discontinuities suggest that nuclei, just like atoms, have a shell structure. This is supported by deviations from the semi-empirical mass formula, the relative abundance of even-even nuclei, neutron capture cross sections, etc. The discontinuities happen at specific values of N and Z, namely 2, 8, 20, 28, 50... these are called magic numbers. ^{16}O is doubly magic, since it has both N and Z equal to 8. As an even-even nucleus, ^{16}O exhibits a ground state with total momentum and parity of $J^\pi = 0^+$. Beyond that ^{16}O has four bound states at excitation energies: 6.05, 6.13, 6.92 and 7.12 MeV with $J^\pi = 0^+$, 3^-, 2^+ and 1^- respectively [8]. The two odd parity states are considered to be single-particle configurations that are well described with the shell model, but the even parity states have been characterized as cluster configurations [6].

Cluster configurations are the result of the very tightly bound nature of the alpha particle. Consisting of two neutrons and two protons, the alpha particle is also doubly magic. The alpha nucleus is the most stable light nucleus, with a much higher average binding energy per nucleon (7.074 MeV) than its nearest neighbors ^{3}He (2.573 MeV) and ^{6}Li (5.332 MeV) [9]. Another testament to its stable nature, is the position of the first excited state, which resides at an impressive 20.21 MeV. The alpha particles also have strong α-α repulsion due to the Pauli exclusion principle, which makes the alpha particle a good candidate for a shell model analog build on the alpha particle instead of the regular nucleons, assuming that some or all of the nucleons combine to form alpha particles that move in orbits in an overall potential [30]. This can then be treated as you would the normal shell model, with eigenvalues and eigenfunctions in the overall potential providing energies and waveforms of the alpha particle states. Applying this to the ^{16}O nucleus yields results remarkably close to experimental findings. Note that in most ground states, the cluster structure does not survive as separate alpha clusters, but the particles are compacted and overlap slightly. The cluster structure becomes most relevant close to the cluster decay thresholds. Most famously the Hoyle state, a 0_2^+ state in ^{12}C at E_x = 7.65 MeV exhibits a three alpha cluster like structure [10]. This is a couple hundred keV above the three alpha breakup threshold at 7.27 MeV. Similar behavior is expected from heavier alpha conjugate nuclei such a ^{16}O or ^{20}Ne.

The separation energy of ^{16}O into the ground state of ^{12}C and an alpha particle corresponds to an excitation energy of 7.16 MeV only a few hundred keV above the 2^+ and 1^- bound states. The four alpha decay threshold, where the nucleus breaks into four individual alpha particles, is located at 14.44 MeV, and possible candidates for this cluster state are the 0^+ states at 13.66 14.03 and 15.10 MeV [11]. The first two states are below the breakup threshold, these are the 0_4^+ and 0_5^+ states, whereas the 0_6^+ state is above the threshold. The validity of the spin assignment of the 0_4^+ state will be brought into question in section 4.4. In 2007 [12] the spin parity of this state is estimated to be a 0^+, but older sources [8] lists this state as a 1^+ which is more consistent with the data presented in section 4.4. The state at 15.10 MeV was shown to be a strong candidate for the cluster state in [11]. This will be explored in more detail during the analysis, more specifically in section 4.5 where attempts are made to confirm this states as a good candidate.

The ^{15}N(p,α_x)^{12}C reaction has a Q-value of 4.965 MeV which is rather large. The reason behind this large Q-value is clear when viewed in the perspective of alpha clustering. The resulting ^{12}C + α can both be seen as made up of an integral number of alpha particles, all of which are tightly bound compared to that of the proton and ^{15}N. An even larger Q-value would be that of the gamma transitioning to the ground state in ^{16}O at a value of 12.13 MeV. For this transition E1 direct capture to the ground state is greatly suppressed, and the large Q-value favors resonance decay instead, however E2 direct capture might become relevant in areas far from any resonances. However, transitions to excited states in ^{16}O have much lower Q-values than those to the ground state, causing direct capture to be on par with resonance decays, even dominating at some points [6]. The cross section of these transitions are expected to be small compared to those to the ground state. A number of these excited states do not allow further gamma decay to the ground state, and are expected to only decay via the alpha channel. The reaction would be as follows,

$$p + {}^{15}N \rightarrow {}^{16}O^* \rightarrow {}^{16}O^* + \gamma \rightarrow \alpha + {}^{12}C + \gamma$$

This would result in lower energy alphas than what would be expected from the ^{15}N(p,α_x)^{12}C reaction alone and from the energies of these alphas, it should be possible to determine the energies of the gammas emitted in the gamma decay.

Transitions to the unbound state 1^- at 9.59 MeV have possibly been seen in 1968 [13]. These should be measurable with our setup along with other possible candidates, and the 1^- is located at an energy very relevant to astrophysical models. This state is one of the two greatest contributors to the low-end cross sections of the $^{12}C(\alpha,\gamma)^{16}O$ reaction, along with the bound 1^- state at 7.12 MeV. This will also be discussed again in the analysis, more specifically in section 4.6.

Now lets add all of this to the levels diagram from figure 1.2. The ground state and alpha threshold was already on there, we recognize that as the α_0, but the bound states, four alpha threshold and possible intermediate states, have been added and can be seen in figure 1.3

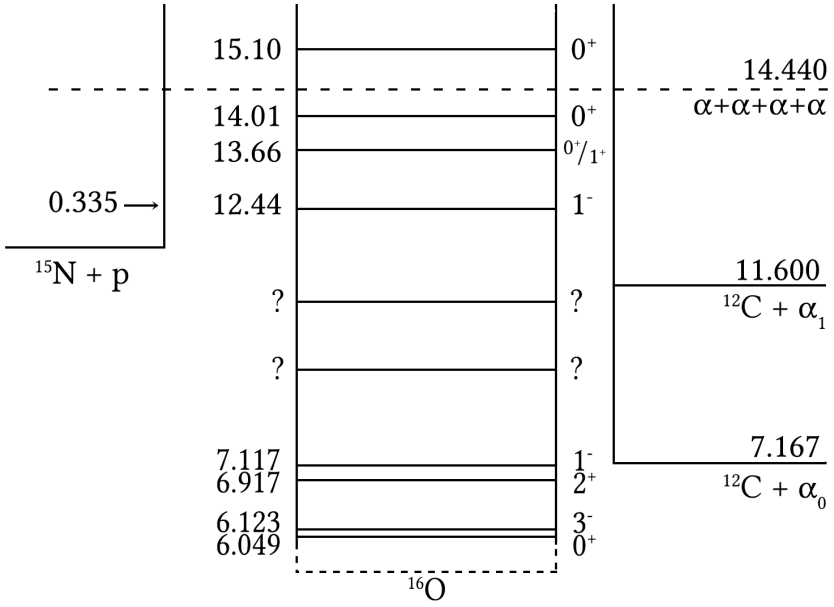

Figure 1.3: *Bound states of ^{16}O, the four alpha threshold and possible intermediate states has been added to figure 1.2. This figure will be expanded once more to encapsulate the entire work presented in this thesis. This can be seen in figure 1.5*

1.3 Nuclear Reactions

The main focus of the experimental work in this thesis, is performing an energy scan of the states in the ^{16}O compound nucleus accessible via the $^{15}N(p,\alpha_x)^{12}C$ reaction

and also within the range of possible proton energy capabilities of the 5 MV Van de Graff facility at Aarhus University, more on this in section 2.1. The experimental work has been carried out in two separate phases, called the IFA022 and the IFA028 experiments. The IFA022 experiment focused on the lower range of proton energies from 331 keV up to a maximum of slightly below 2 MeV. Energies higher than 2 MeV were not accessible at the time of the IFA022 experiment, due to a gas leak in the pressure vessel containing the belt of the Van de Graff. This leak prevented the vessel from being pressurized with SF_6 gas, which due to a higher dielectric breakdown allows more charge on the belt before sparking to the sides of the pressure vessel. The IFA022 experiment was carried out from October to November of 2017.

The IFA028 experiment started in the March of 2018 and ran well into April of 2018. Here the gas leak had been fixed and energies as high as 4000 keV were possible. The IFA028 experiment includes energies from 2000 to 3800 keV, with the majority of runs having proton energies exceeding 2900 keV, since ^{16}O is not reported to have any states in the region from 2000 to 2900 keV. A table of every single run carried out during both experiments, along with proton energies and duration, can be found in appendix A and B. A detailed list of all states in the ^{16}O compound nucleus will be provided in chapter 4.

Cross Sections

Once the energy scan is completed, the level structure of ^{16}O can be examined in detail by calculating the cross section of the reaction at every point of the scan. Expressing this as a function of either beam or excitation energy will provide a detailed picture of the ^{16}O nucleus.

The cross section, denoted by σ, is a proportional to the probability that an interaction will occur. In figure 1.4 an illustration of the beam impacting a target is available. The beam consists of N_b ingoing particles per unit time t. The beam has an area of A. The target is made up of N_t target nuclei, and the number of reactions occurring during the time t is N_R/t. N_R is assumed to be equal to the number of emitted particles N_e. The cross section of this reaction is defined as the number of interactions per unit time, divided by number of incident particles per unit time per unit area, times the number of target nuclei within the beam [14]. In terms of the

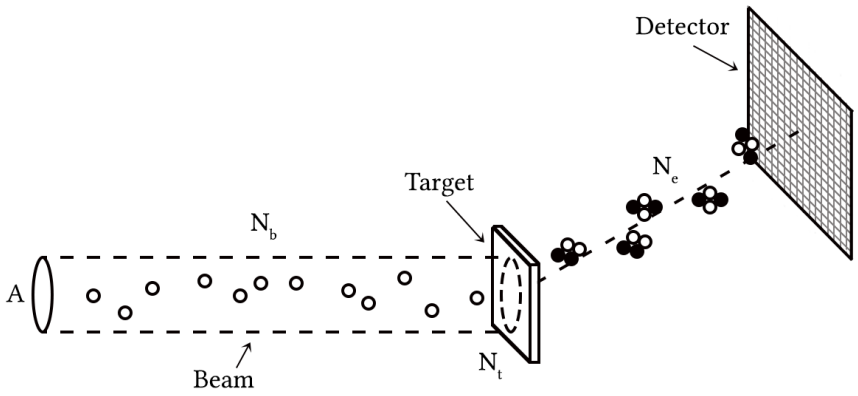

Figure 1.4: *Illustration of a typical nuclear reaction experiment. A beam of N_b particles impacts a target, and the following reaction emits N_e particles. Figure inspired by figure 2.1 in [14].*

illustration we get,

$$\sigma \equiv \frac{N_R/t}{(N_b/tA)\cdot N_t}. \tag{1.1}$$

Or in terms of emitted particles, the number of emitted particles per unit time is,

$$\frac{N_e}{t} = \frac{N_b}{tA}\cdot N_t \cdot \sigma. \tag{1.2}$$

We will express this slightly different in the analysis in chapter 4. Here we present the total number of emitted particles, which would be called the yield. This is the amount of detected particles that fit the criteria for the reaction of interest. The number of beam particles is expressed in terms of integrated beam current. A small counter in the beam line records every time a set amount of current has passed and passes on the value TRUE. The number of TRUE pulses can be counted and from this number the beam current can be inferred. By taking the charge of the beam particle into account, the number of incident particles can be determined. The total number of target nuclei is calculated as the density of the target, times the thickness of the target and andavogadro's number divided by the molar mass of the target nuclei. This would mean that the yield, N, can be expressed as,

$$N = \frac{IC}{q\cdot e}\cdot \rho\Delta t\frac{N_a}{m}\cdot\sigma. \tag{1.3}$$

A setup used for detecting the emitted particles will never detect every single particle due to various effects. The above expression must take this into account. One effect is the detector dead time, DT. This is time where the detectors are not reading. Obviously if the detectors are off, particles will escape detection, this has to be accounted for. Another thing is the overall efficiency of the detector setup, this will be discussed in detail in section 4.3, but for now, we will just denote it ϵ, a number between 0 and 1. With these additions the total yield becomes,

$$N = \frac{IC}{q \cdot e} \cdot \rho \Delta t \frac{N_a}{m} \cdot \sigma \cdot DT \cdot \epsilon, \tag{1.4}$$

and the cross section of a reaction will thus be given as,

$$\sigma = \frac{q \cdot e}{IC} \cdot \frac{m}{\rho \Delta t N_a} \cdot \frac{N}{DT \cdot \epsilon}. \tag{1.5}$$

This will be used extensively in the analysis, and the reaction cross sections of α_0 and α_1 as a function of excitation energy can be seen in figures 4.14 and 4.15.

The Breit-Wigner formula

As described in the previous section, the measured cross section will have contributions from multiple ^{16}O resonances. In order to extract tentative values for their positions and widths, a suitable parameterization of the resonance line shape is needed. Such a parameterization is the so called Breit-Wigner formula that relates the total cross section to the resonance width and energy. The formula takes the form,

$$\sigma = \frac{\pi}{k^2}(2l+1)\frac{\Gamma^2}{(E_s - E)^2 + \Gamma^2/4}, \tag{1.6}$$

where E is the energy, E_s is the resonance energy and Γ is the width of the resonance. When fitting the $\frac{\pi}{k^2}(2l+1)$ term is simply treated as a constant divided by energy.

This should provide a good basis for treatment of isolated peaks, but in areas where resonances are interfering it will not be able to tell the full story. As we shall see in the analysis, this treatment was relatively successful at even extracting values of up to three resonances in very close proximity. The correct treatment would be to perform R-matrix analysis of the data, but that is beyond the scope of this thesis, even though the ground work has been thoroughly laid, as will be presented in the angular distribution analysis.

1.4 Motivation

Let us now complete the expansion of the levels diagram. We include the full range of the energy scan with the most energetic resonance at 3.50 MeV. The final diagram can be seen in figure 1.5.

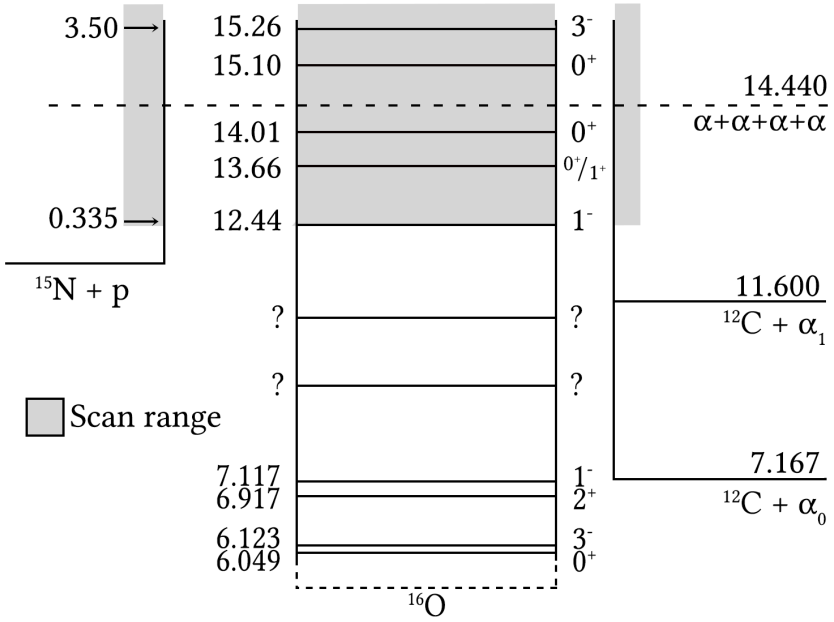

Figure 1.5: *The energy scan range is now included in the level diagram, and it is now complete. This figure is and expanded version of 1.2 and 1.3.*

By now it should be evident that all parts of this thesis will focus on building information about the level structure of ^{16}O. The energy scan in particular will provide detailed information on the different states. The same can be said for the predicted gamma transitions and the possible detection of the four alpha cluster state. Though these are more specific to singular states, whereas the scan tries to encompass everything. If sufficient information is collected, a more advanced analysis of the states will be possible, and the accuracy in the position and width of each state can be improved. As mentioned earlier, direct measurements of reaction cross sections relevant for stellar energies are impossible in the present day. Therefore extrapolations to these energies are necessary, and the accuracy of these extrapolation

are extremely dependent on the accurate description of states at higher energies. In order to perform the extrapolation, a model of the achievable states is of course needed. This will likely be an R-matrix fit, and when performing more advanced analyses, such as an R-matrix fit, multiple different reaction channels are often included and many background levels added. The precision of the fit strongly depends on the information put into it, making all information valuable. A scan as vast as the one performed in this thesis has never been carried out before, and the information we can expect from it, especially in the high energy range that has not been examined in detail earlier, will be extremely valuable to future analyses.

The endpoint of the analysis in this thesis will be providing input data for an R-matrix analysis. This will take the form of angular distributions in the energy range from 300 keV to 3800 keV. A simpler analysis using the Breit-Wigner formula will also be performed to estimate the results of the analysis without diving into an R-matrix analysis.

Chapter 2

Experimental Methods

The focus of this chapter will be on explaining the experimental setup used during the course of this thesis. Both of the IFA022 and IFA028 experiments were carried out at the 5 MV Accelerator facility at Aarhus University. This facility will be presented in the first section. The two sections following that will focus on the detector setup used and the manufacturing of the CN-targets, since both of these are very important aspects to consider during the analysis. The remainder of this chapter will focus on relaying data from the detectors to some safe storage and also what happens to the data signals on the way to safe storage.

2.1 The 5 MV Accelerator facility at Aarhus University

All of the experimental work presented in this thesis have been carried out at the 5 MV Van de Graff accelerator at the Department of Physics and Astronomy at Aarhus University. The accelerator is a standard Van de Graff accelerator setup, relying on a rotating belt to build up an electrostatic charge that is used to accelerate charged particles along a linear path. This beam of accelerated particles is guided through a series of slits and steerers until it arrives at the reaction chamber, where it impacts with the target material. Inside the reaction chamber resides an array of carefully constructed detectors, whose sole purpose is to relay information about the reactions taking place within the chamber. This information is then carried away and processed by the data acquisition system (DAQ). A detailed illustration of the 5 MV accelerator facility can be found in figure 2.1.

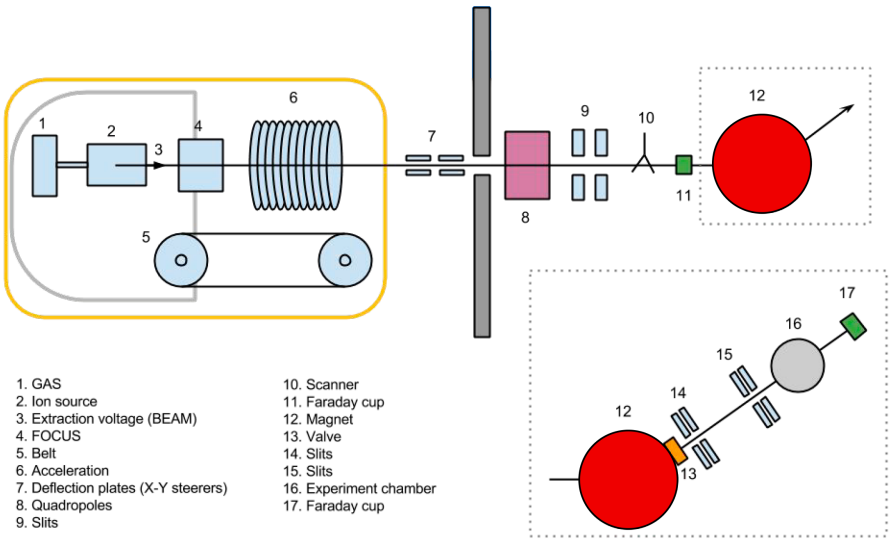

Figure 2.1: *A detailed schematic of the 5 MV accelerator facility. Everything within the yellow line, numbers 1 through 6, is contained within the large pressure vessel. The gray bars denote a concrete wall and numbers 13 and above is part of the specific subatomic beam line. Figure courtesy of Oliver Kirsebom*

Van de Graff accelerators are typically placed inside large pressurized vessels, as the large electrostatic buildup, makes sparks from the dome to the surroundings very likely to happen. By placing the accelerator under pressure, the potential for sparks greatly decreases. According to Paschen's Law, the breakdown potential within a gas increases linearly with pressure, making this a favorable choice. The breakdown potential also depends on the composition of the gas, which is why an atmosphere of sulfur hexafluoride is usually preferred [15]. A mixture of nitrogen and carbon dioxide (80 % N_2 and 20 % CO_2) is also sometimes used.

All accelerators exploit the Lorentz force, which states that charged particles move in the presence of an electromagnetic field, to accelerate particles. Hence the acceleration starts with an ion source, which is placed within the pressurized tank. The ion source produces ions via a RF-field, which due to the higher mobility of the electrons, strips the gas and leaves behind a positively charged plasma. The ion source at the 5 MV facility can produce a number of different ions, the prominent ones being H^+, H_2^+, H_3^+, $^3He^+$ and $^4He^+$. The plasma is then carried away by a small extraction potential, commonly referred to as BEAM within the group. A rather

neat looking image of the ignited ion source can be seen in figure 2.2. In this figure, one of the two rings providing the extraction potential is also visible along with the a number of the focusing elements, referred to as FOCUS.

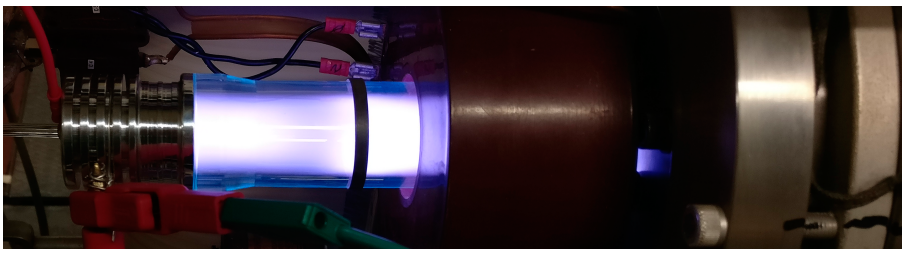

Figure 2.2: *A picture of the ignited ion source. An even more viewer friendly version of this photo, can be found as a video on YouTube, courtesy of Frank Daugaard from the electronics department [16].*

After the beam of charged particles exits the ion source they enter the acceleration tube. The acceleration tube is constructed of an insulating material with vacuum tight seals to metal electrodes. The vacuum seals are very important due to the high pressure environment outside the tube compared to the very low pressure within the tube. The electrodes of the tube are connected to the dome of the Van de Graff generator and provide an accelerating and focusing electric field for the beam of charged particles. The dome is electrolytically charged via a motorized belt rubbing against a comb of metallic wires connected to a DC voltage supply. Once the beam leaves the acceleration tube, it encounters a set of deflection plates, a quadrapole, some slits, a beam scanner and a removable Faraday cup, before entering the magnetic bending stage. All of these elements are used to ensure a stable and controllable beam.

The magnetic bending stage is made up of a large dipole electromagnet, that allows very precise selection of a certain mass to charge ratio ion beam. The current going to the magnet can be adjusted manually and the group has developed a formula for estimating the current needed to get the desired beam, which can then be optimized even further at a later stage. Before the beam enters the reaction chamber, it passes through another series of slits for final adjusting. After the reaction chamber resides another Faraday cup which is placed within a 1 m beam pipe [17] in order to reduce the amount of beam backscattered into the chamber. The reaction chamber

contains two very crucial elements of the setup, namely; the detectors and the target. The following two sections will be dedicated to describing each of these individually.

2.2 The Detector Setup

The detecting system is extremely important in experimental nuclear physics. It is very possible to have a successful experiment, but with no detection system, how would anyone know? Joking aside, the system utilized in the IFA022 and IFA028 experiments was made up of two different detector types, two annular Double-sided Silicon Strip Detectors, (DSSD), and two quadratic DSSDs. Each of the two detector types can be seen to the right in figure 2.3, and a schematic drawing of all detectors can be seen in the middle of figure 2.3.

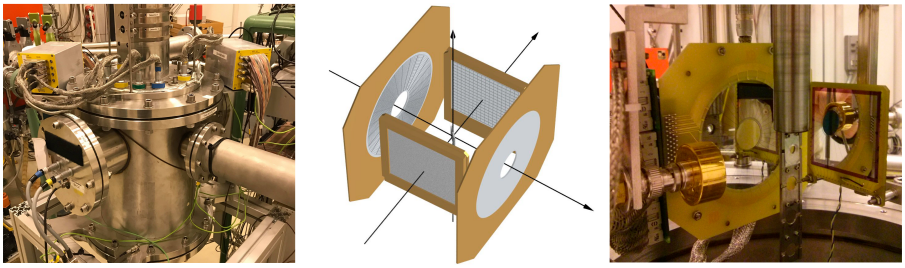

Figure 2.3: ***Left:*** *The reaction chamber and electronics viewed from outside.* ***Right:*** *The detector setup and target ladder removed from the chamber but still in correct orientation.* ***Middle:*** *A schematic drawing of the detector setup. The setup consists of two annular S3 detectors and two quadratic W1 detectors. The beam enters through the upstream S3 detector, impacts the target in the center of the chamber and exits either through the detectors or the hole in the downstream S3 detector.*

The two quadratic DSSD are of the type W1 [18]. They are located 40 mm from the target center, one to the right and one to the left with respect to the beam direction. Each detector has an active area of 50 by 50 mm^2 divided into 16 individual strips both on the front and back [19]. All strips has a surface area of 3 by 50 mm^2, making the detector have a 256 pixel grid made up of 3 by 3 mm^2 squares. The front side is p^+-doped to a depth of 100 nm and is covered by a grid of aluminum contacts covering up 2 % of the front surface. The back side is n^+-doped to a depth of 400 nm and covered by a 200 nm thick conducting Aluminum layer. The thin front layer in combination with the grid of aluminum contacts ensures the smallest

possible inactive layer before particles can interacting with the bulk material. No such caution is necessary on the back side of the detector, which is why the entire surface is covered with a conducting layer. The total thickness of each W1 detector is approximately 60 µm.

The S3 annular detectors share many of the same features, however instead of strips, the S3's have 32 spokes on the front and 24 rings on the back. The radial distance from the inner to the outer active area is 24 mm, making the rings + aluminum contacts 1 mm wide. The spokes vary in width from 4.3 mm at the inner most ring to 13.7 mm at the outer most ring. The S3 detectors have a larger inactive layer than the W1 detectors, with a value roughly 5 times larger, ∼500 nm. The S3 detectors are placed either 36 mm upstream or downstream from the target.

From now on, the upstream detector, will be referred to as SU and the downstream detector as SD. The two quadratic detectors will normally not need individual names, as they cover the same angular range. Thus, they will be referred to simply as the W's. If individual naming is needed for the W's, they will be referred to as DET1 and DET2. DET1 is to the left as seen in regards to beam direction, DET2 is to the right. An overview of the two different types of DSSDs can be seen in figure 2.4.

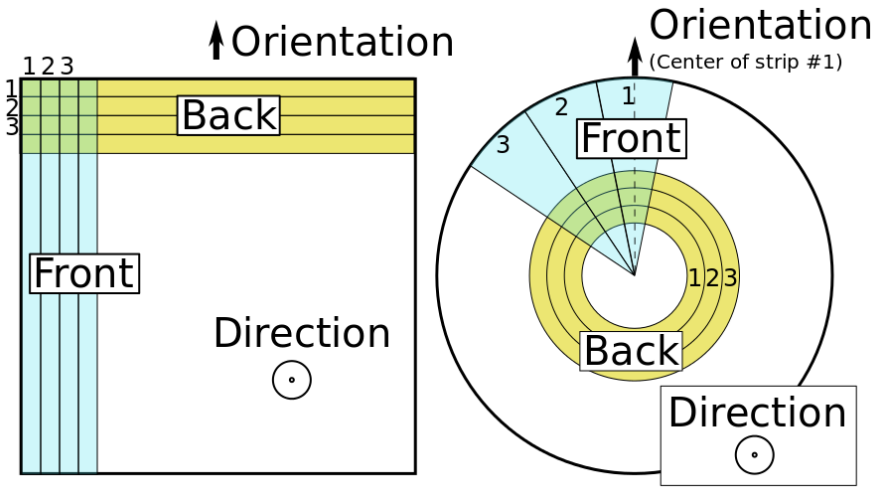

Figure 2.4: *The layout of the W's can be seen to the left. Each W detector has 16 strips on front and back. The layout of the S3's can be seen on the right. Each S3 detector has 32 spokes on the front and 24 rings on the back.*

Most silicon detectors work by doping a small strip of silicon, essentially turning them into diodes and applying a bias. In semiconductor detectors ionizing radiation from the reaction penetrates the detectors and creates charge carriers in the form of electron hole pairs. The bias on the detector collects the electrons and holes at opposite ends of the detectors where the charge is collected. The number of electron hole pairs produced by the radiation is proportional to the incoming energy, meaning that the energy of an incoming particle can be inferred from the charge buildup in the detector. All four detectors have a small inactive dead layer on the surface. This layer will naturally lower the energy of any incoming particles and this loss of energy can become quite significant. The incoming energy is also affected by the angle of the incoming particle, since this effectively increases the size of the dead layer. For a given α particle with energy, E, arriving at an angle ϕ, the detected energy, E', will be,

$$E' = E - \frac{\Delta}{|\cos\phi|}\frac{dE}{dx}, \tag{2.1}$$

where Δ is the thickness of the dead layer. For a 3 MeV α particle hitting straight on, this corresponds to a 96 keV shift in energy, which is massive when a precision of a few keV is expected. Naturally, this is a problem a simple calibration can solve, which at the 5 MV facility is performed via a 1 kBq source containing ^{148}Gd, ^{239}Pu and ^{244}Cm. These isotopes have very well defined narrow peaks, and calibrations performed with this method are self consistent within $\sim$2 keV.

The reaction chamber can be seen from the outside to the left in figure 2.3, and the beam line extending out to the last Faraday cup is visible on the right side of that photo. During the IFA022 experiment the target was kept at a 45° angle with respect to the beam, while SD was kept at 0°, SU at 180° and the W's at $\pm$90°. The angle of the target effectively increases the target thickness, an effect that has to be accounted for in the setup. During the IFA028 experiment, all parameters were kept the same, except the W detectors were rotated 5° leaving them at 95° and 85° respectively. This was done to combat the target ladder causing shadowing on the outer edges of the detectors.

2.3 Making the CN-Targets

In order to probe the ^{16}O nucleus through the ^{15}N(p,α)^{12}C reaction, a ^{15}N target is of great importance. In the following section the production of the ^{15}N targets via radio frequency magnetron sputtering will be described, and the physical properties of the target will be listed at the end. Procedures and production methods explained in the following section are based on [20] and [21].

Radio Frequency Magnetron Sputtering

Radio Frequency Magnetron Sputtering (RF-MS) is a plasma-assisted technique used to deposit thin films onto a substrate. The basic premise of RF-MS is to transfer material from a target onto a substrate. Used correctly, the material will be deposited as a thin film on the substrate. The energy needed to transfer material from the target to the substrate is generated by slamming plasma ions into the target surface, causing target material to sputter out. The plasma is generated by applying an electric field to a working gas inside a sputtering chamber. This gas is typically a noble gas of a similar atomic mass to the target material. With a target material of carbon, the working gas of choice is argon. When the electric field is applied to the argon gas, any stray electrons will be accelerated by the field. This promotes collisions with the working gas and results in the gas becoming ionized,

$$e^- + Ar \rightarrow 2e^- + Ar^+.$$

Once this collision has occurred, an additional electron and an argon ion are also available to assist in the ionization. This quickly turns into a cascade reaction, causing the entirety of the working gas to be ionized effectively. In RF-MS this ionization is additionally stimulated by alternating the electric field. This is done in such a manner that the electrons receive a boost of energy from the changing field, and provides much easier ionization than what is found in DC counterparts.

A basic schematic of a sputtering chamber can be seen in figure 2.5. The chamber in the figure is set up in such a way as to sputter a mixture of carbon and nitrogen onto a carbon substrate. At the top of the chamber a carbon substrate is placed and at the bottom, a carbon target. The chamber is pumped with a mixture of argon and very pure ^{15}N.

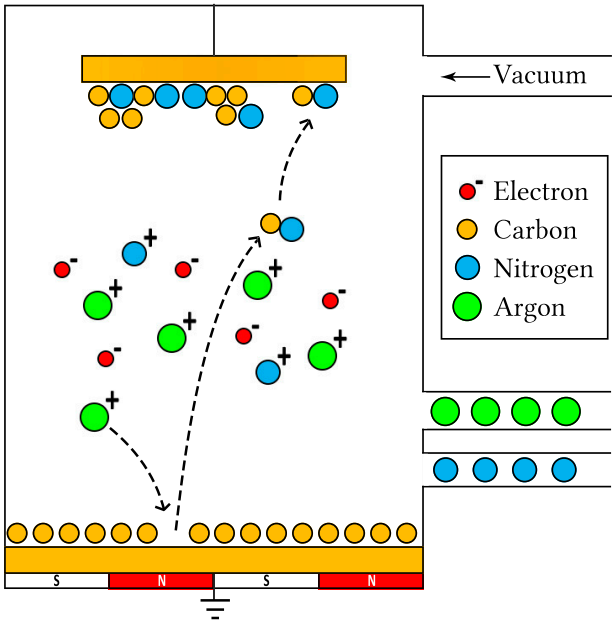

Figure 2.5: *A basic schematic of a sputtering chamber. argon plasma is created by an electric field. Argon ions are used to sputter carbon atoms from the target surface. Sputtered carbon atoms react with nitrogen atoms and bond to the surface of the substrate, forming a thin film of CN.*

Once the ionization of the working gas is complete and the plasma is stable, essentially every wall inside the chamber will be negatively charged. Since electrons have higher mobility compared to the working gas ions, more electrons will reach the chamber surfaces during the positive part of the RF potential cycle, than ions during the negative part, providing a self-biasing effect to everything within the chamber. The positive ions of the working gas will now start bombarding the negatively charged target surface. Ions impacting the surface transfer their energy to the carbon atoms on the surface of the target through momentum transfer reactions. Given enough energy, this will result in the ejection, or sputtering, of target atoms. These ejected carbon atoms have a neutral charge and pass through the plasma, where they react with the nitrogen gas and eventually get deposited on all chamber surfaces, including the substrate. In RF-MS, powerful permanent magnets are placed below the target material in order to confine charged plasma particles close to the sputtering surface which in turn increases sputtering yield. Electrons follow a helical path in

the presence of strong magnetic fields. This means an increase of effective path length, causing more ionization close to the sputtering surface. As mentioned the sputtered atoms are mostly neutral and also much heavier, so they pass unaffected through this magnetic trap. Sputtering from ion-bombardment generally occur at energies from $10^{-2} - 10^{4}$ eV.

RF-MS tuning parameters

Atoms on the surface of the substrate are also subject to bombardment, even with the strong magnetic traps surrounding the target material, which attempts to confine the plasma. The bombardment of the substrate seems unwanted, as attempts are made to build up material on the surface of the substrate, not the opposite. However, bombardment of the substrate surface can cause rearrangement of the surface atoms and might even resputter less tightly bound atoms resulting in a smoother surface. Thus properties such as crystallinity, grain size and morphology of the surface can be modified by controlling the ion-bombardment of the substrate. To control this, several parameters can be adjusted. The most influential of these are discussed below.

Substrate temperature: The temperature of the substrate is very important as it affects the nucleation rate and diffusion of atoms on the surface. Increasing the temperature, increases the critical size of the nucleons and the nucleation barrier. This allows for a slower deposition of nuclei and larger crystalline structures, meaning af denser material is created with less defects.

Substrate bias: Higher substrate bias means more energetic bombardment of the surface. This will increase the mobility of the surface atoms and result in a smoother surface, but might also introduce defects and even embed argon atom in the material.

Pressure: The effect of chamber pressure is very similar to the effect of substrate bias. Less pressure in the chamber allows for more energetic ions, and results are the same as above.

Sputtering power: The sputtering power affects the number and energy of ions hitting the target, which provide an easy way to control the deposition rate. More power means higher deposition, but a higher deposition rate allows less time for atoms to find low energy equilibrium sites on the surface, before being bound by additional impinging ions. Too high deposition rates can thus result in a porous

material.

Base vacuum: A good base vacuum is critical in order to ensure minimal contaminants in the chamber, and many chambers are baked throughly before introducing the working gas.

Physical Properties of the CN-targets

Two batches of targets were produced. The first batch in the summer of 2017 and the second in the spring of 2018. An example of a target can be seen on figure 2.6. The target is made up of a thin CN-film placed on a metal target holder. The film is so thin that it is transparent, and it requires careful treatment. Exhaling too close to the target might break the film.

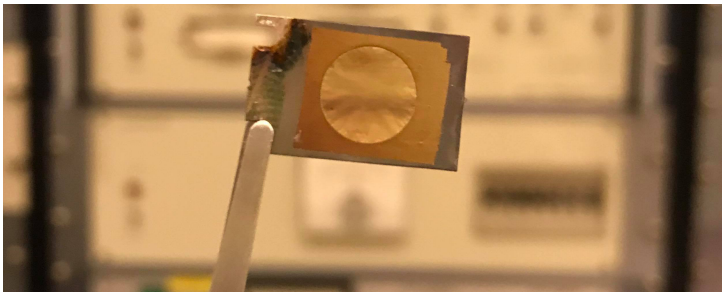

Figure 2.6: *An example of a CN-target. The thin film made from sputtering carbon and nitrogen onto a carbon substrate is placed on a metal target holder.*

The targets all share the same properties and are regarded as identical. The substrate is made of ^{12}C and has a surface density of 4 μg/cm^2, value provided by manufacture [22]. Assuming a density of 2 g/cm^3, the substrate thickness becomes 20 nm. Sputtered onto the substrate is a thin film of carbon and ^{15}N in a ratio of 40 % nitrogen and 60 % carbon. The surface density of the CN-films were produced to be 20 μg/cm^2 with an estimated uncertainty of less than 5 % [22]. Values were determined by Rutherford Back Scattering (RBS) performed on the targets [23]. A total of 10 CN-targets were produced, 5 in each batch.

2.4 Data Acquisition System

The data acquisition system (DAQ) is responsible for translating the very small signals from electron hole pair production in the silicon detectors into high quality digital data. At the 5 MV facility in Aarhus, the DAQ can be divided into three parts: The analog chain, the digital chain and the readout system, each of which have their function depicted in figure 2.7.

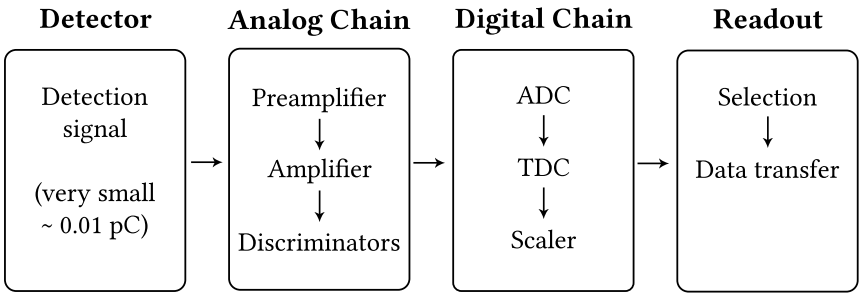

Figure 2.7: *A schematic representation of the data acquisition system. The signal from the detectors is passed though a number of amplifiers and discriminators. After this, an ADC and a TDC converts the signal to a digital one, that is subjected to some selection criteria, and then passed on to secure and permanent storage.*

The signals from the silicon detectors are very small. At room temperature, a silicon detector will on average produce E/3.62 eV electron hole pairs [24]. This is equivalent to 0.01 - 0.2 pC with the beam energies utilized during the IFA022 and IFA028 experiments. This is a *very* small signal, and it is of great importance that the amplification happens very close to the signal source, since such a small signal is very susceptible to noise.

The Analog Chain

As such, a preamplifier will be the first step in the analog chain, followed by a secondary amplifier and then a series of discriminators. The preamp works by integrating the current on a capacitor. This simultaneously converts the charge signal to a voltage signal, which is still proportional with the deposited particle energy. This stage requires a small buffer to recharge the capacitor and sets a hard limit on the output rate. The secondary amplification introduces an adjustable

gain and shapes the signal. The last step is used for selecting interesting signals. The discriminators employ two different techniques, leading edge detection and a constant fraction discriminator (CFD). The first discards low amplitude signals which are mainly due to noise and the second finds the position of the maximum of each detection. Both conveniently also provide signals for time stamping.

The Digital Chain

In the second chain, the digital one, an analog-to-digital converter (ADC), converts the analog signal into a digital value for the amplitude size. This is again proportional to the deposited energy. A time-to-digital converter (TDC) takes the signal from the discriminators and timestamps all incoming pulses. Lastly, a scaler is used to measure the amount of beam particles hitting the target. This is done by a beam digitizer, which outputs a true logic signal for each 10 pC it measures. These signals can then be summed and used to scale the data. A number of different modules are used for the steps in this chain, and they all have different busy times. The overshadowing one is the ADC which requires 5.7 µs for each event. This, together with the amplification buffer, sets a hard limit of roughly 100 kHz maximum detection rate.

The Readout system

The readout system is responsible for transferring the data from the data acquisition modules (DAMs) to some safe and persistent storage. In the case of the IFA022 and IFA028 experiments, the focus is a multi-particle final state, meaning that events are only interesting if multiple detectors are firing. However, a downscaled amount of single particle date is also of interest. An AND condition between detectors ensures multi-detector events, and a downscaled single-detector event is done by simply accepting every N^{th} trigger.

2.5 A Brief Overview of AUSAlib

Experiments within the branch of nuclear physics contain huge amounts of data and it is impossible for a human being to manually analyze everything. To make this process much more manageable, computer programs are used to do the majority of

the work. One such framework of computer programs is AUSAlib [25]. AUSAlib stands for "Aarhus University Subatomic Library". The library has been developed mainly by Michael Munch [26] from the Subatomic group at the Department of Physics and Astronomy at Aarhus University. A very brief overview of AUSAlib will be presented in the following, but more parts of it will be explained in greater detail in chapter 3.

AUSAlib was developed to streamline and unify the process from raw data to analysis. All the different aspects of AUSAlib utilized in this thesis can be found in figure 2.8.

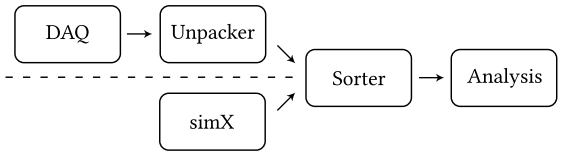

Figure 2.8: *A schematic representation of the process from data to analysis. Data from the DAQ is unpacked and then passed through a Sorter after which it is ready for analysis. Simulations performed by simX can also be passed through the same Sorter and will yield a similar data structure for analysis.*

Two different methods can be used to obtain data which can be processed via AUSAlib. One of which is of course an experiment, with the other being a simulation of said experiment. AUSAlib provides tools to recreate the entirety of an experimental setup, and then allows the user to run either real physical data through, or to simulate data with a program called simX and run that through the same analysis. Simulations are of great use, as they allow the user to check for potential errors and also prepare for upcoming experiments by allowing optimization of the detector geometry, without physically carrying out the experiment. The simX program requires a description of the desired nuclear reaction, properties of the beam and a setup file compatible with AUSAlib. From this, simX can generate root files with a similar structure to the real world data once they have been send through the unpacker.

When handling raw data from the DAQ, the first step would be to pass the data though the unpacker. This unpacker takes the data and sorts it neatly into root files. Each event would have its own TBranches within the TTree of the root file. This structure will be mimicked by the simulated files from simX, and from now on they

can be treated equally.

The data, now arranged in root files, still have energies expressed in terms of a number between 0 and 4096 and furthermore, it is not currently known what hits on the front and back of the DSSDs form a pair. The Sorter program performs solves both of these by performing calibrations and matching. The Sorter requires knowledge of the setup and also a matcher file declaring low energy cuts, tolerance and TDC offsets. Once the data has been passed through the Sorter, the user will be left with a root file containing information about multiplicity, energy, time and identity (location on the detector where the particle hit) of each and every event in the file. With this, analysis can be performed on the data. The analysis will be very experiment dependent and will not be discussed further in this chapter, however AUSAlib does provide a number of tools useful for analysis.

Chapter 3

Data Reduction

The majority of the work presented in this thesis is processed through the cross platform C++ framework called ROOT [27]. ROOT was created at CERN in 1995 by René Brun and Fons Rademakers and was initially a private project, but has since grown to be the dominant analysis toolkit used at the Large Hadron Collider and most other particle and nuclear laboratories. ROOT is built to handle large amounts of data, a characteristic of most nuclear physics. Experiments usually consists of many events with identical data structure, which are assumed to be statistically independent. These events will all require complementary information in order to be analyzed, such as detector or beam parameters. This information does not change at an event scale, but only on a run specific scale where a run is defined as set of events with constant settings. ROOT allows the user to access these events selectively. This is crucial.

A very common task in nuclear physics data analysis is selectively accessing single-event data. Traditional database management systems partition data horizontally, which does not allow for selective scanning on an event scale. ROOT partitions data vertically in what is known as TTrees. Each TTree is partitioned into TBranches. A TBranch stores consecutive objects, data members or even other TBranches. When reading data stored in a TBranch, the structure of the TTree allows for reading only that TBranch. This structure is what allows ROOT to efficiently handle larges amounts of data.

In the upcoming sections we will follow these large amounts of data from the

DAQ to the unpacked stage, then through the Sorter and into the Analysis programs, with a series of examples along the way. Every single runs obtained as part of this thesis has been passed through the Unpacker, Sorter and some version of the Analyzer. At the end of this chapter, the Simulator is also briefly presented. The Simulator provides an alternative way of generating unpacked data, that will prove very powerful in the upcoming analysis.

3.1 Unpacked Files

In the IFA022 and IFA028 experiments, an event is triggered every time a detector reads a signal larger than the trigger threshold value. After this trigger, an event is initialized, and all detector signals within a predefined time period are stored in that event. The AUSAlib Unpacker converts these raw data files into ROOT files, these will be called the unpacked files. Each event has its own set of TBranches that are stored within the TTree which defines the run. Each tree of the unpacked files contains the following branches:

SU_R	SD_R	DET1F	DET2F
SU_RI	SD_RI	DET1FI	DET2FI
SU_R_E	SD_R_E	DET1F_E	DET2F_E
SU_R_T	SD_R_T	DET1F_T	DET2F_T
SU_S	SD_S	DET1B	DET2B
SU_SI	SD_SI	DET1BI	DET2BI
SU_S_E	SD_S_E	DET1B_E	DET2B_E
SU_S_T	SD_S_T	DET1B_T	DET2B_T

There is a clear repeating pattern in the naming of these branches. Each column is divided into one of the four detectors, **SU**, **SD**, **DET1** and **DET2**. Every detector has a front and a back side, these are named **F**, (front) and **B**, (back) on the W's and **S** (front) and **R** (back) on the S3's, since these have spokes on the front and rings on the back. The tree is then further subdivided into four categories, multiplicity, identity **I**, energy **_E** and time **_T**. Storing the data like this, facilitates the use of zero suppression which is considerably more storage efficient. With this in mind, the

branch containing the energy deposited in the back side of DET1 would be called DET1B_E. An entire event for a single detector could look like this:

```
DET1F     = 2          // Two hits on the front
DET1FI    = [3,5]      // Strips 3 and 5 were hit
DET1F_E   = [525,725]  // Energy 525 impacted strip 3, 725 in strip 5
DET1F_T   = [250,600]  // Strip 3 was hit at time 250, strip 5 at time 600
————————
DET1B     = 2          // Two hits on the back
DET1BI    = [3,5]      // Strips 3 and 5 were hit
DET1B_E   = [500,700]  // Energy 500 impacted strip 3, 700 in strip 5
DET1B_T   = [250,600]  // Strip 3 was hit at time 250, strip 5 at time 600
```

From this it is evident that the front side of DET1 was hit two times, on strips 3 and 5. The energy that was deposited in strip 3 was 525, and the energy in strip 5 was 725. In the unpacked files the energy is stored as a value between 0 and 4096, since it is a 12-bit ADC, meaning that it does not have an appropriate unit of energy yet. For now, these numbers will be refered to as channel numbers. It is also clear that strip 3 was hit at time 250, and strip 5 at time 600. Time has the unit of 100 ps which is determined by the discriminators. The backside of DET1 will have a similar structure, as we have seen above.

Already with the unpacked files some rough analysis can be performed. A single run from the IFA022 experiment, with protons hitting that target with an energy of 1210 keV, will be used for this. Plotting the number of counts as a function of deposited energy yields figure 3.1. This figure shows energy deposited in a single strip, in this case strip 13 on the front side of DET1.

Two distinct peaks are visible, one at a much higher energy than the other. Given the large Q-value of the ^{15}N(p,α_0)^{12}C reaction (Q = 4.965 MeV), the high energy peak cannot be anything other than the α_0 reaction. The other peak is a mixture of proton scattering, the carbon atoms and also α_1, which unfortunately share the same energy range. With this, the matched files, obtained via the Sorter, will be the next step in the reduction process.

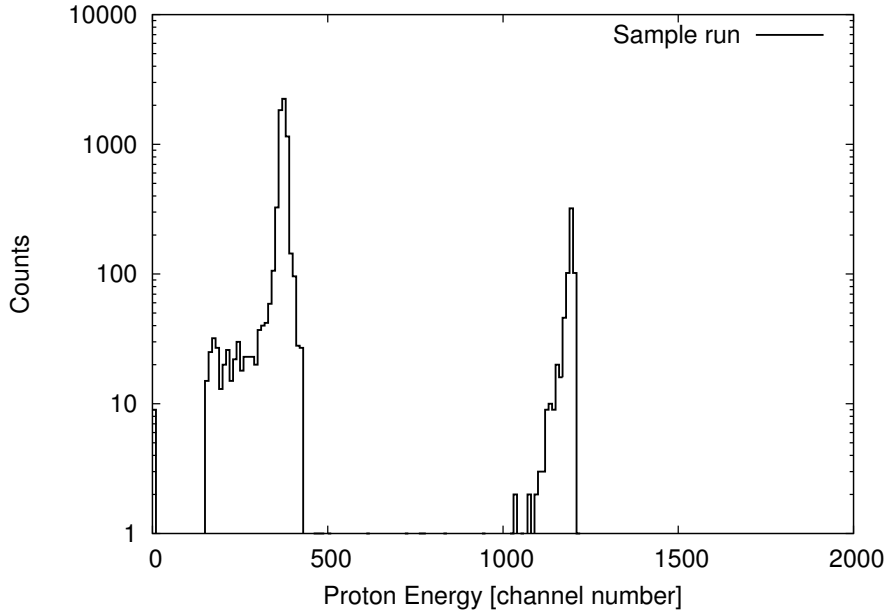

Figure 3.1: *Counts as a function of deposited energy in strip 13 on the front of DET1 in the IFA022 experiment. Data is from run 2506 at a proton energy of 1210 keV. Two peaks can be seen. Highest is α_0s and lowest a mixture of the beam, ^{12}C, and α_1*

3.2 Matched Files

Since all four detectors in the setup are DSSDs, a large problem with the unpacked files is that it is not known, which hits on the front and back forms a pair. It will also be necessary to translate pixel positions into angles. But first, we need to tackle the energy calibration, since this will have to be applied before the matching is performed.

Energy Calibration

Energy calibrations are performed using yet another tool from AUSAlib. This tool will be referred to as the Calibrator. The Calibrator takes a number of inputs, many of which have default settings. Let us have a quick rundown of the different stages of the calibration. Firstly, the tool needs an input file containing a measurement of a known source. These sources can be specified manually. In figure 3.2 the different steps of the calibration have been applied to the triple alpha source mentioned in

section 2.2.

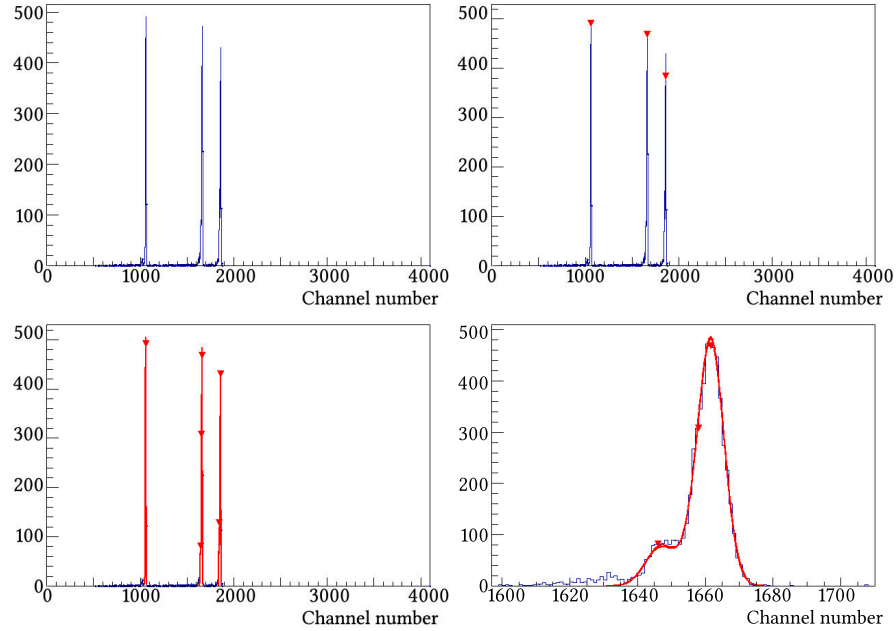

Figure 3.2: *The different steps of creating an energy calibration. The example here is using a triple alpha source containing ^{148}Gd, ^{239}Pu and ^{244}Cm. The top right histogram shows the three main peaks. The top left shows each of these peaks identified by a rough fitting routine, and the two bottom histograms show the detailed fit which includes sub-peaks and a zoom of that.*

This source has three main peaks and a number of lower intensity sub peaks. The energy of these peaks has to be know, and they should be contained within the specified source file. On the top left corner of figure 3.2 , three main peaks are clearly visible. The first step will be to roughly determine the position of each of the three main peaks. This can be seen in the top right corner of figure 3.2, where each of the three peaks have been identified. This is done by identifying the highest peak, and then excluding all channels within $\pm W/2$, where W is a used specified width around the identified peak. Once this has identified the number of main peaks specified in the source file, a more detailed fitting routine runs on each of the main peaks. This utilizes a Gaussian routine and fits the sub-peaks as well. This is seen in the bottom left of 3.2, and a zoom of the middle peak is included on the bottom right. The zoom allows us to see the main peak along with two sub-peaks indicated by the

red downwards pointing arrows. The rough fit provides no estimate of error, but the second fit uses a Gaussian fit to estimate errors. The fitting routine uses the peak centroids from the previous fit as a first guess and the fitting region is $\pm 3\sigma$. Note that the fits are carried out individually for each isotope. Once the Calibrator is run, the output will contain a .cal file that holds calibration coefficients in two columns. The first is energy offset and the second is the slope.

Geometry Calibration

Another calibration tool is the Geometry Fitter, once again a tool provided by AUSAlib. The Geometry Fitter provides two options, an Isotropic Geometry Fitter and a Polynomial Geometry Fitter. We will be utilizing the Isotropic Geometry Fitter. In order to perform the geometry calibration, a rough energy calibration must first be obtained. This is easily obtained by running the Calibrator discussed above, once before the Geometry Fitter and once after the Geometry Fitter. This will provide the best results. The Geometry Fitter assumes that the hitpattern originates from an isotropic distribution, meaning that the number of counts in a pixel is proportional to its solid angle,

$$N(i,j) = C\Omega(i,j), \tag{3.1}$$

where C is just a constant. The solid angle, $\Omega(i,j)$ is approximated as,

$$\Omega(i,j) = A\frac{|\hat{n}\cdot\hat{r}(i,j)|}{r^2(i,j)}. \tag{3.2}$$

Fitting this model to the calibration data an estimate for the detector positions can be determined. Once this is calibrated, the energy calibration can be performed again by running the Sorter mentioned in section 2.5 to yield a more accurate result. The updates position improves the energy loss calculations performed in the energy calibration, thus improving the overall result of the energy calibration.

Matching

Once the energy calibration is in place, we can return to the problem of matching. Let us use the example event from before. On the front side, a 525 and a 725 energy particle impacted strip 3 and 5 respectively, and on the back side a 500 and a 700 energy particle impacted strip 3 and 5 respectively. This means that we have two

different combinations of pairs. This situation is illustrated in figure 3.3. Each hit is marked with an X, and the two possible combination of pairs are marked in red and green. In order to perform matching, a simple algorithm is applied, which selects the

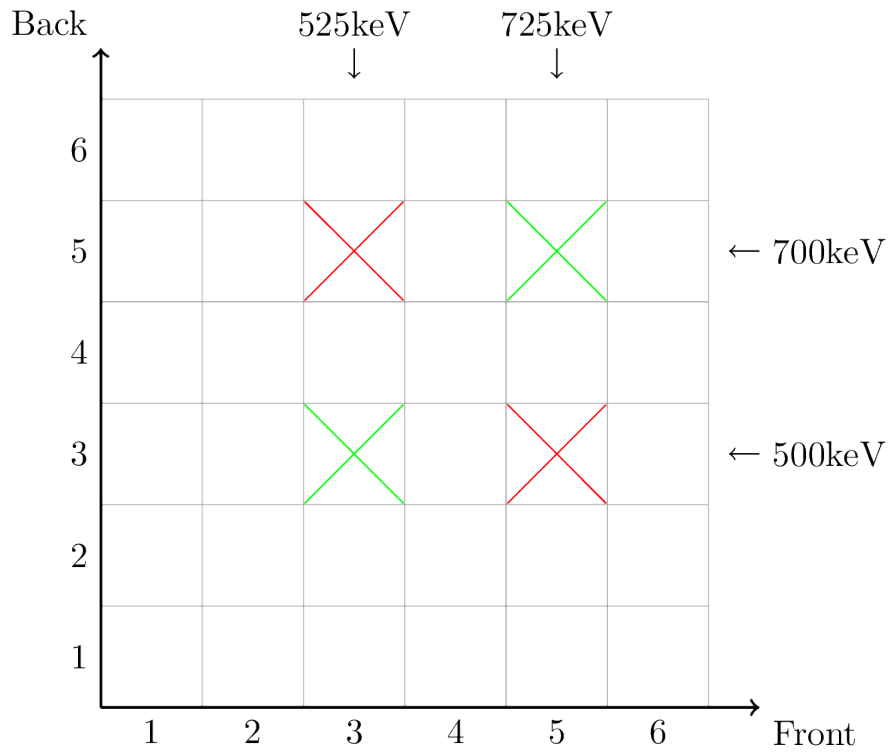

Figure 3.3: *A 6x6 grid representing a small detectors. Two particles have impacted the front at energies* 525 keV *and* 725 keV *and the back at energies* 500 keV *and* 700 keV*. Pairs are selected from least energy difference, and the best match is highlighted in green. Figure courtesy of Michael Munch [26]*

pairs with lowest difference between front and back. With this in mind, matching would select (3,3) and (5,5) as pairs. Both of these are marked in green.

The Sorter

The energy calibration plus matching has to be applied to all runs, and have been combined in the Sorter tool from AUSAlib, which was briefly mentioned above and in section 2.5. The Sorter takes a number of input files. These inputs are required to run the Sorter. They contain information that is not event specific, but constant

during a run and sorting will not be possible without them. Focus will be on two of these inputs, as they are the most relevant for the experiments performed in this thesis. These are the setup file and the matcher file.

The user can specify a number of these inputs within the matcher file. The matcher file used for the IFA022 and IFA028 experiments contains information about the energy tolerance, that is, the maximum allowed energy difference between front and back pairs that are matched. It also specifies information about a lower cut. This is a way to enforce a lower boundary on what signals will go through. Both of these values are kept at 100 keV during the entirety of this thesis. This means that particles with an energy less than 100 keV will not make it through the Sorter, and no matching will be performed if the energy difference is more than 100 keV. In the matcher file it is also possible to specify a TDC offset and disable a number of strips on a specific detector. TDC offsets are applied to each side of a detector and must be held within a file specifying; strip number, offset and standard deviation. TDC offsets are used to calibrate time between channels. These might differ due to different cable lengths, discriminators, etc. Turning off specific strips of a detector is done via a disable command within the matcher file and this will prove very useful later on, since almost every single detector will have some strips turned off during the IFA022 and IFA028 experiments. This will be discussed further in section 4.1.

The setup files store information on what detectors are used in the experiment. It tells AUSAlib about the detector's name, calibrations, position and orientation. The energy calibration file from the Calibrator is provided to the setup file, along with information on position from the geometry calibration. Once all of this is in place, we are ready to harvest the power of the Sorter. The TTree of a sorted file will contain the following branches,

FI	FE	FT	mul	phi
BI	BE	BT	theta	id

Clearly the branches have changed from the unpacked files. This is due to all detectors now being combined, instead of having their own 2x4 branches. It is still possible to determine what detector an event is from, accessible with the new **id** branch. More specific information about spatial distribution of the events, has also been

gained in the form of the theta and phi branches. Other than that, it is still the same multiplicity, identity, energy and time branches that were available in the unpacked files. Repeating the same rough analysis on the single run at 1210 keV from IFA022, plotting counts as a function of deposited energy in strip 13 on the front of DET1. This can be seen in figure 3.4.

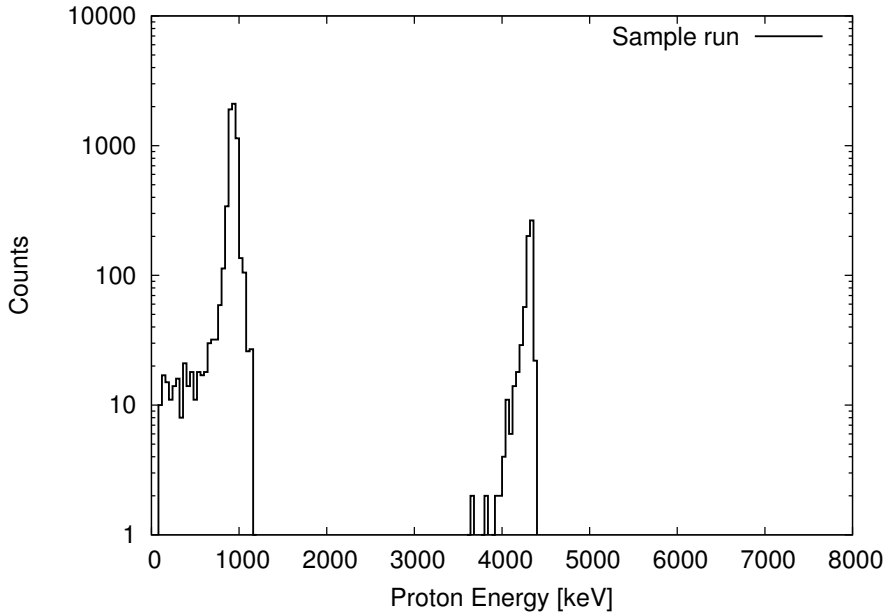

Figure 3.4: *Counts as a function of deposited energy in strip 13 on the front of DET1 in the IFA022 experiment. Data is from run 2506 at a proton energy of 1210 keV. This has been passed through the Sorter, and energy is now in keV.*

This is essentially the same plot as the one in figure 3.1, however as expected, the calibrations and the low cut are now in effect. Since the branch FE now contains all hits on the front side, it would now also be possible to do a sum plot, where all hits on the front of DET1 are shown, instead of only strip 13. This will drastically increase the number of counts, easily by one order of magnitude, since we would be looking at all sixteen strips instead of just one. This will become relevant since we now intend to move on to a rough analysis of the data. Here we will no longer distinguish between what strips a particle hit only what detector it hit.

3.3 Analyzed Files

The next step will be to roughly outline the two analysis programs written for this thesis. The purpose of the analysis is to combine the individual detector hits into physical events. That means it will calculate physical properties of the detected particles such as momentum, center of mass calculations, excitation energies etc. This will form the basis for more targeted data analysis in chapter 4. Both of the programs discussed below this are originally written by Michael Munch and then modified for the IFA022 and IFA028 experiments.

Doubles Analysis

This analysis focuses on identifying the carbon and the alpha particles from the reaction. The analyzer looks for events with more than one hit, demands that these hits are in different detectors to avoid self coincidences and that hits need to happen within 100 ns of each other in order to confirm they do form a pair. The analysis then assigns the highest energy particle to be the alpha particle and the other to be the ^{12}C. Subsequently it corrects for energy losses in the dead layer on the detectors and energy loss within the target. Both of these corrections depend on the setup and target geometry, which is provided by the setup and target input files. Once energy loss calculations are in place, the analyzer performs the necessary calculations to output a ROOT file containing the following branches:

mul	pC	pA
dP	vC	vA
Pcm	vCcm	vAcm
V	DEC	DEA
ex	EC	EA
	ECcm	EAcm
	TC	TA
	iC	iA

These branches are divided into five event specific branches and eight particle specific branches. The event specific branches are multiplicity, total momentum, center of

mass momentum, total angle and excitation energy of ^{16}O. These are listed in the left column. The particle specific branches are, particle momentum, angle, center of mass angle, deposited energy, energy, center of mass energy, time and identity, where both the carbon and alpha particle will have their own branches. All momentum branches are three dimensional vectors with spatial components.

As we have done with the unpacked- and sorted files, we may now also make a plot of counts versus energy. Since we no longer have all energies combined in one branch, but instead energies of the carbon and alpha particles, the plot will be somewhat different from the last two. We choose to plot the energy of the alphas and we may even plot the center of mass energies to narrow the peaks even further. We will not bother resolving what angular ranges strip 13 of DET1 corresponds to, but instead plot all hits on DET1. This should result in an increase of counts. The plot can be seen in figure 3.5.

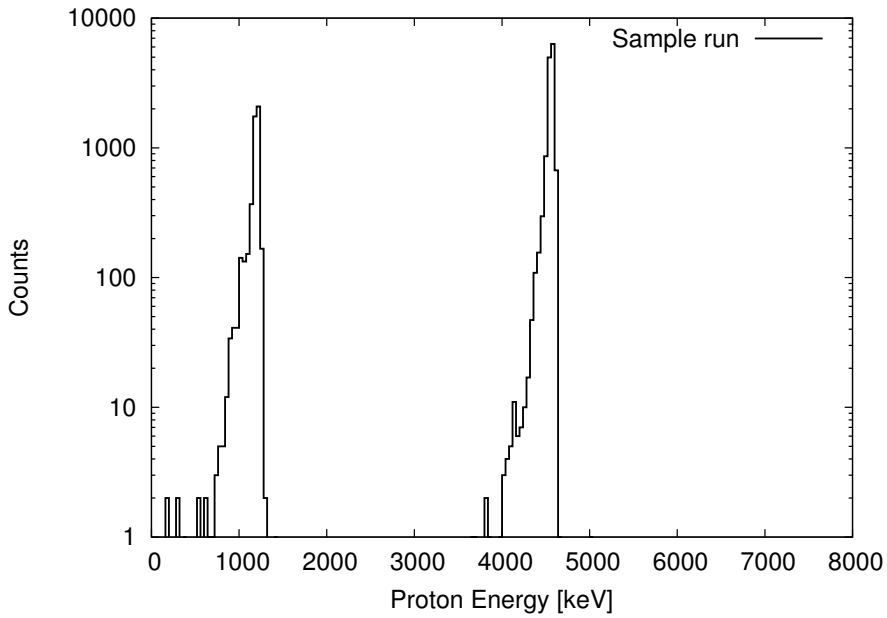

Figure 3.5: *Counts as a function of alpha particle energy. Only DET1 hits are included. Data is from run 2506 at a proton energy of 1210 keV. This has been passed through the Doubles analysis and energy is now corrected for energy loss in the target and detector dead layer.*

Looking at figure 3.5 we see for the first time that α_0 has a higher number of

counts than α_1. This was not possible to tell earlier on, since α_1 was grouped with carbon and scattered protons. This is also consistent with what we would expect at a beam energy of 1210 keV, since we are populating a 3^- state in ^{16}O that is resonant in both, α_0 and α_1, but couples more strongly to the α_0 channel [8].

Singles Analysis

The Singles analysis is based on the same framework as the Doubles analysis, though here, as the name suggests, every hit is included meaning no demands on multiplicity. The purpose of the Singles analysis is to compute center of mass quantities such as energy and theta for all hits, assuming they all correspond to the alpha particle of the ^{15}N(p,α_0) reaction. The Singles analysis contains the following branches:

E	V	Vcos	Vleft
kin	Vcm	Vcoscm	Vright

The branches are, energy, kinematic curves, angle, center of mass angle, angle in cos, center of mass angle in cos plus left and right angles. As before, we can plot the counts at each energy. This can be seen in figure 3.6.

This plot is more reminiscent of what we had in section 3.1 and 3.2. Again α_0 is obvious at $\sim$ 4500 keV, but a bit more definition has been provided at lower energies. We see scattered protons forming the largest peak. The small front peak at $\sim$ 1400 keV is the ground state carbon atoms and the lowest peak at $\sim$ 300 keV is the excited state carbon atoms. The kinematic curves reveal that α_1 is somewhat encapsulated by the scattered proton peak, but the shoulder barely visible on the front of the peak, should be caused by α_1.

The Simulator – simX

The simulator is an extremely powerful tool from AUSAlib [28]. The simulator tool is called simX and consists of an easy to use framework that makes Monte Carlo simulations of nuclear reactions using the setup from the actual experiment. Like most of AUSAlib, simX is built on C++. SimX requires a configuration file containing information on detection setup, the beam, the target and the reaction. The detection

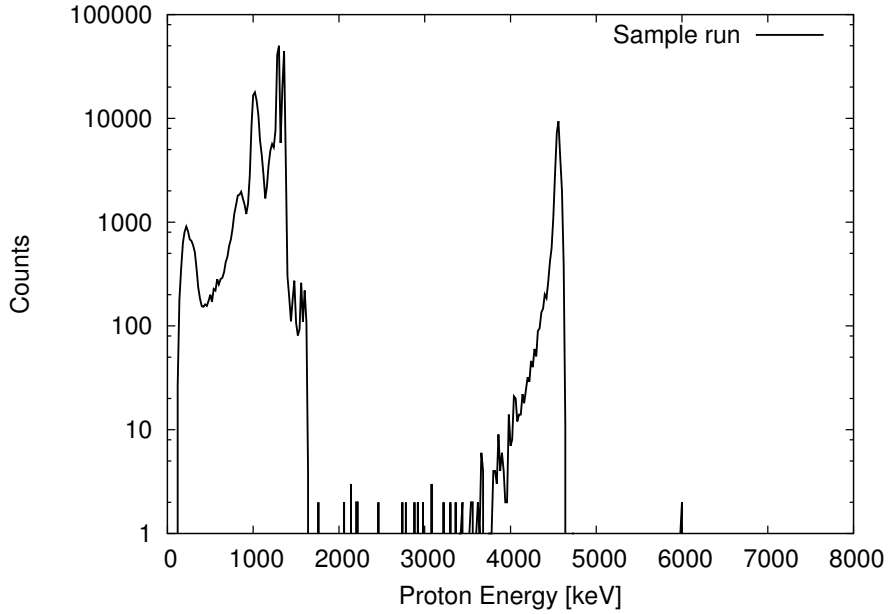

Figure 3.6: *Counts as a function of alpha particle energy. Only DET1 hits are included. Data is from run 2506 at a proton energy of 1210 keV. This has been passed through the Singles analysis and energy is now corrected for energy loss in the target and detector dead layer.*

setup will just point to the setup files also used by the Sorter, since these two have to match for it to provide an accurate simulation. The beam file specifies energy, center position and angle of the beam, along with some options for choosing whether to use a point sized beam or not. Beam energy, along with a number of other things can also be specified as a flag once the simulation is run, a feature that is quite handy when running multiple simulations. The target file holds information about the materials of the target, thickness and orientation. The most interesting input is the reaction file. Let us have a look at what two reaction files might look like for a simulation of the ^{15}N(p,α_x)^{12}C reaction:

```
beam: p
target: N15
-> {
    a
    12C
}
```

```
beam: p
target: N15
-> {
    a
    12C Ex: 4438keV
}
```

On the left we have the α_0 decay and on the right the α_1 decay. As we see these files are rather simple. They require the ingoing particle, target and then the outgoing particles. If we run either one of these through simX with the rest of the configuration in place, then the output of this simulation will be a ROOT file that can be treated as any unpacked file, since they will have the same structure. Let us plot this like we did the unpacked file, front energy of strip 13 on DET1. The simulation will be that of α_0 and the plot can be viewed in figure 3.7.

Since this is a simulation, this is the most easy-to-read plot so far. We see two peaks, one is the alpha particles and the other one ^{12}C. The alphas have the most energy, so that will be the highest energy peak. It is also good to see the two peaks lining up with those of the real data from figure 3.1. Since this is in principle an unpacked file. Energy is not yet calibrated and this file can be put through the Sorter and any analysis code. The power of the simulator comes from it allowing us to determine the detection efficiencies of the experimental setup and run experiments without actually running them. This can be used to provide information on setups even before they are built, and help guide their optimization.

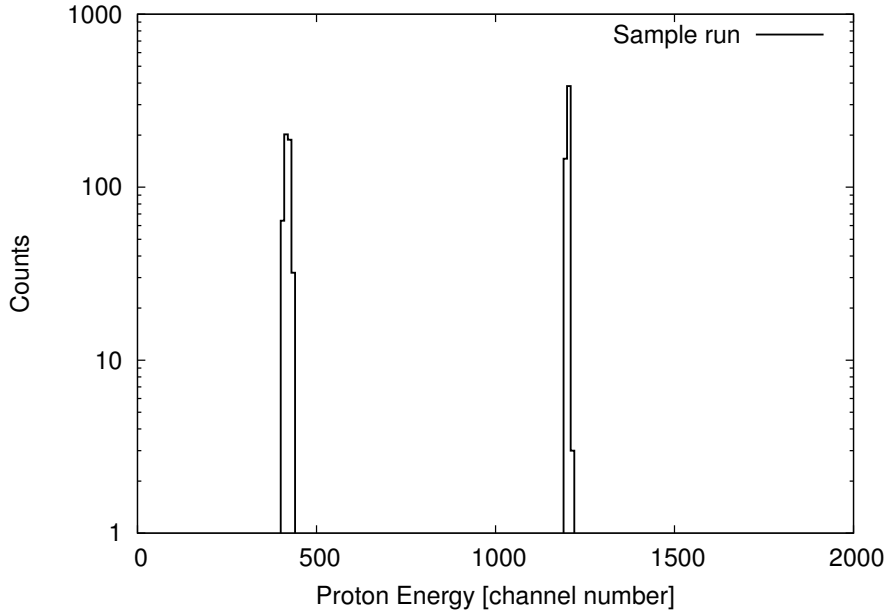

Figure 3.7: *In this figure a simulated run of the $^{15}N(p,\alpha_x)^{12}C$ reaction is plotted. The simulation was carried out using the setup from the IFA022 experiment. Counts are plotted as a function of channel number.*

Chapter 4

Data Analysis and Results

During the IFA022 and IFA028 experiments 81.3 GB of data has been obtained. This is distributed among 102 runs in IFA022 and $\sim$ 32 hours of running combined with 112 runs in IFA028 and $\sim$ 73 hours of running. Proton energies vary from 331 keV to 3800 keV and the average run time is 26 minutes. In between every single run, the beam had to be re-tuned and set up for another run. IFA022 focuses on the lower end of proton energies from 331 keV to 2000 keV and IFA028 the higher end from 2000 keV to 3800 keV. All runs were carried out using the same setup with few exceptions, one being a new batch of targets for the IFA028 experiment. However, as far as the data produced, these targets are considered to be identical to the ones used in the IFA022 experiment. Different strips on the DSSDs were also disabled in the IFA028 experiment compared to that of IFA022. This will be elaborated in the upcoming section. The energy of all runs from both experiments have been plotted in figure 4.1 to provide a quick overview of the energy scan.

Every run performed in both experiments can be found in the appendix A and B with information on run number, energy and duration. All proposed states of ^{16}O, along with proton energies and J^{π}, can be found on the left side of table 4.3 [8].

Each of the 214 runs performed during the IFA022 and IFA028 experiments were carefully chosen to provide information on each of the states from table 4.3. This is why figure 4.1 does not show equally spaced energy intervals. More measurements were performed closer to known resonances in order to maximize information available on each resonance. In off-resonance areas, for example the area from 2000

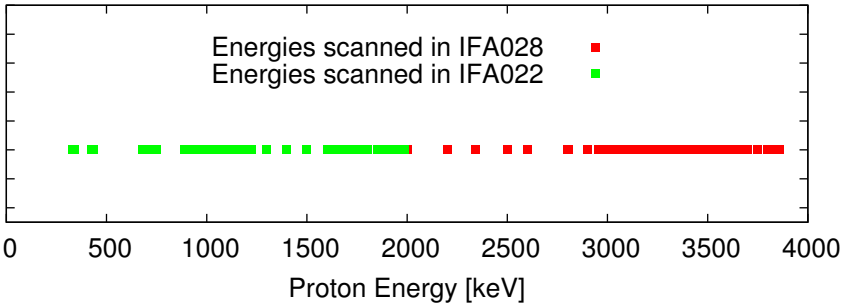

Figure 4.1: *Energy range of the scans performed in IFA022 and IFA028.*

to 3000 keV, fewer and more spaced out measurements were performed.

The upcoming sections will deal with the different aspects of the analysis performed throughout this thesis. The primary focus will be on the energy scan, but sections dedicated to exploring the four alpha breakup channel and possible gamma transitions, have also been included. However, first we will discuss the state of the detector setup for each of the two IFA experiments. The two annular S3 detectors, SD in particular, had peculiarities during both of the experiments. In the IFA028 experiment, some additional strips had to be turned off compared to IFA022.

4.1 Tuning the Detectors

The matcher file allows us to turn off certain strips of the detectors when using the Sorter. This is rather useful for the analysis, since some strips displayed strange behavior. Recall that we have four detectors, all DSSDs, two square detectors with 16 x 16 strips called DET1 and DET2 and two annular detectors with 24 rings and 32 spokes called SD and SU. Additionally we have also included a collimator in the reaction chamber for the IFA022 and IFA028 experiments. The collimator limits the number of hits on SD and preserves the detector. The collimator is made from a threaded tube that extends from the center of SD and into the chamber along the path of the beam. The collimator can be extended or retracted to block incoming particles bound to hit SD. The closer we move the collimator to the target, the more rings on SD are blocked, starting with the inner-most rings. This has been put in place to ensure the longevity of the SD detector, since this experiences significantly

more radiation damage and therefore gets worn down fastest.

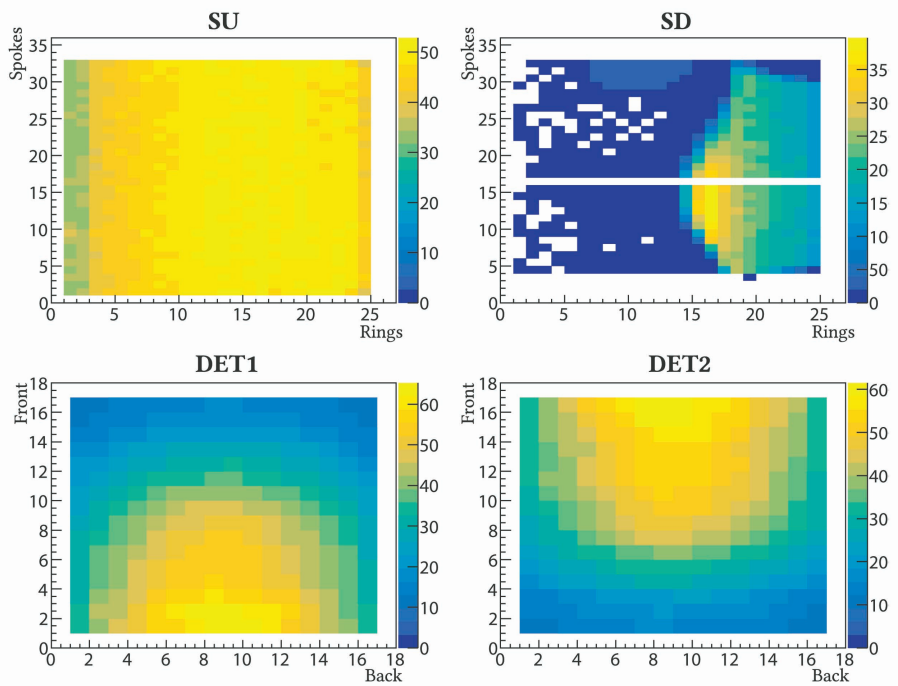

Figure 4.2: *Hit patterns of the four detectors SU, SD, DET1 and DET2, used in the IFA022 setup. Hit patterns are from run number 2500 at a beam energy of 1210 keV*

In figure 4.2 the hit patterns of all four detectors have been plotted. This plot is from run 2500 in the IFA022 experiment and was carried out at a beam energy of 1210 keV. All strips are active in this plot.

At first glance SU seems to have a uniform distribution of hits, which is very good, since this is what we are expecting from SU. The spokes are very uniform in appearance and the rings seem to gradually increase slightly in number of hits, which is also expected. On SD the effect of the collimator is very clear. The inner rings are all receiving close to no counts, meaning the collimator is working as intended. The beam also seems to have been slightly off center. When tuning the beam, it is very difficult to get it exactly centered and what we see here is an effect of not achieving that entirely. At the 5 MV facility a small fluorescent screen is located on the target ladder which can be moved into the path of the beam. This, along with a rough hit pattern of SD, is used to tune the beam. It is evident that spokes 1, 2

and 3 are not firing. This is a well-known issue. Spoke 16 also contains no data and must be dead, which was not known prior to the IFA022 experiment. Both of the W's are looking as expected. Run 2500 is very representative of the remainder of the IFA022 experiments. To confirm this, hit patterns from different runs of the IFA022 experiment are included in Appendix C.

From figure 4.2 we can establish some strips to exclude from the analysis. SU looks like it was expected, no action is taken here immediately. It is good practice to turn off the outer strips on the W's to avoid particles entering at an angle and then exiting out the side of the detector. Therefore the outer most strips on the W's will be disabled. SD needs a bit more work. Spokes 1,2,3 and 16 have already been discussed and should clearly be disabled. The strips 4, 31 and 32 have also been disabled as they seem to also be affected by the strips 1, 2 and 3 not firing. With regards to rings, we have to disable everything that should be blocked by the collimator. This has been estimated to be rings 1 through 18. The remaining strips of the detectors, is what we will consider the IFA022 setup. This information is available in table 4.1.

Table 4.1: *Table of the three detector setups used during the IFA022 and IFA028 experiments.*

Setup:	SU	SD	DET1	DET2
IFA022	-	Spokes: 1-4, 16, 31, 32	Front: 1, 16	Front: 1, 16
	-	Rings: 1-18	Back: 1, 16	Back: 1, 16
IFA028	-	Spokes: All	Front: 1, 16	Front: 1, 16
	-	Rings: All	Back: 1, 16	Back: 1, 16
IFA028	Spokes 1-16	Spokes: All	Front: 1, 16	Front: 1, 16
special	-	Rings: All	Back: 1, 16	Back: 1, 16

In the IFA028 experiment, hit patterns is shown in figure 4.3. SU is still behaving nicely and the W's look like what we would expect. SD however seems to be experiencing some issues. This is mainly due to the difficulty in tuning the beam. This beam tuning issue became more of an issue in the IFA028 experiment. Parts of SD may be salvageable through multiplicity cuts and the coincidence triggers, but as a rough cut all of SD has been removed from the setup and it will be explicitly stated if SD is included. These conditions are what we have called the IFA028 setup in table 4.1.

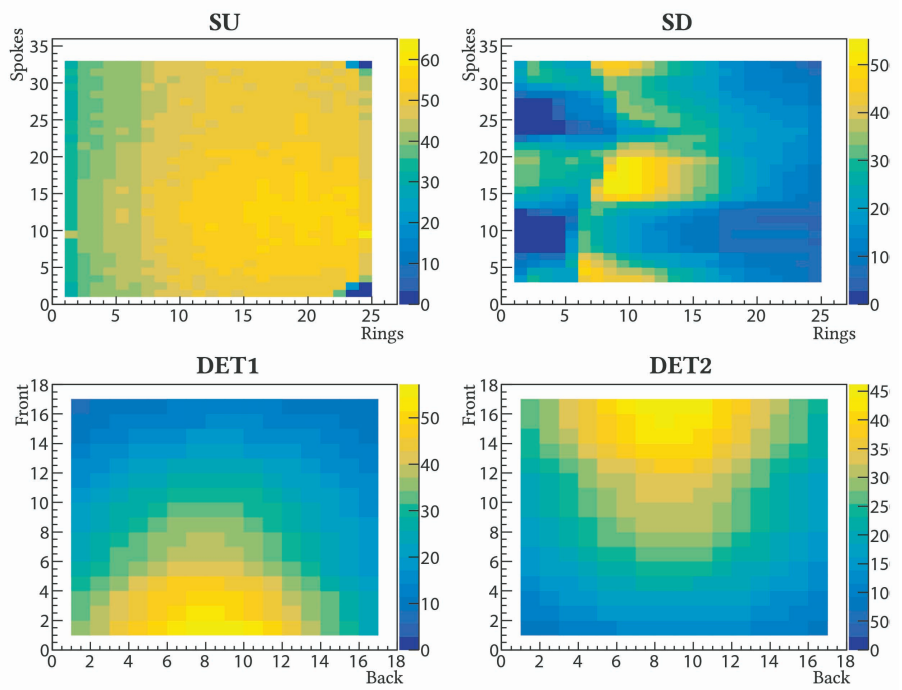

Figure 4.3: *Hit patterns of the four detectors SU, SD, DET1 and DET2, used in the IFA028 setup. Hit patterns are from run number 2863 at a beam energy of 3570 keV*

It has also been necessary to create an additional setup for IFA028, since only runs between March 28th and April 12th conform to the IFA028 normal. This corresponds to run numbers 2800 to 2863. All earlier and subsequent runs in IFA028 are missing the lower 16 strips in SU, due to what presumably is an electronics error. This includes run numbers from 2758 to 2799 and 2864 to 2877. An example of this can be seen in appendix D. This setup has been named IFA028 special, and is also to be found in table 4.1

These setups will be used in the remainder of the analysis, and we will now move on to collecting the yields of α_0 and α_1.

4.2 Yields of α_0 and α_1

To determine yields of α_0 and α_1, events need to be distinguishable from the background. In order to make this possible, we aim to put some constraints on the data,

which only the two alpha reactions will fulfill. Let us have a look at the excitation energy in a single run (run 2500) at a beam energy of 1210 keV, after this run has been passed through the Unpacker, Sorter and Doubles Analysis. This has been plotted in figure 4.4.

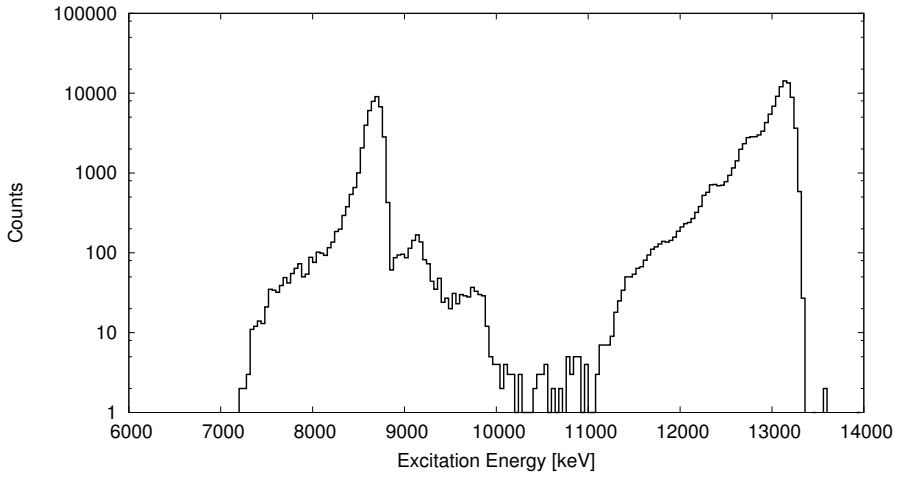

Figure 4.4: *Excitation energies of run 2500 at a proton energy of 1210 keV. No cuts are enforced yet and α_0 and α_1 are hard to resolve.*

At this level it is hard to resolve the peaks of the two alpha reactions. In order to assist in the identification of the position of the two peaks, it seems logical to calculate where we expect them to be. We know that the p + ^{15}N reaction has a Q-value of 12.13 MeV to the ground state of ^{16}O, see figure 1.5. This means that the total energy available for the α + ^{12}C channel will be that Q-value plus whatever energy the proton enters with. We can recalculate this to total energy after the reaction has occurred. The total kinetic energy in the center-of-mass system after the p + ^{15}N reaction is given by

$$E_{tot} = Q + E_p \left(1 - \frac{m_p}{m_p + m_{15N}}\right). \tag{4.1}$$

This means that we expect to see the alphas at the following energies,

$$\alpha_0 = 12\,130\,\text{keV} + E_p \cdot 15/16, \tag{4.2}$$

$$\alpha_1 = 12\,130\,\text{keV} + E_p \cdot 15/16 - 4433\,\text{keV}, \tag{4.3}$$

since the first excited state of ^{12}C sits 4439 keV above the ground state. At a proton energy of 1210 keV this yields E_x = 13 260 keV for α_0 and E_x = 8831 keV for α_1. This is in good agreement with figure 4.4, but it is not enough to select only the desired events.

We will place our first cut, using the V branch which contains the total angle of the outgoing particles. We expect the outgoing particles to be emitted nearly back-to-back, implying a relative angle close to 180°. In order to determine a sufficient cut, total angle, that is the angle between the two ejectiles, at three different beam energies was plotted in figure 4.5.

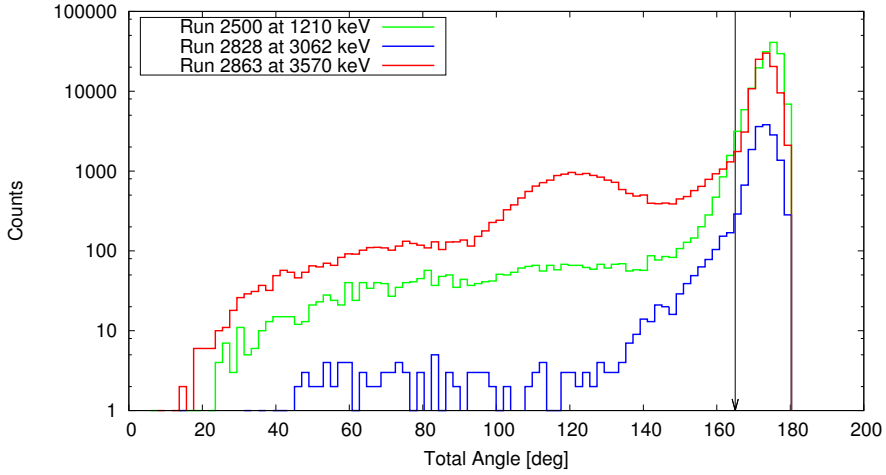

Figure 4.5: *Histogram of total angle in three different runs, 2500, 2828 and 2863. Something close to back to back is expected and a cut is placed at V = 165*

Most events are indeed close to 180 degrees, but as expected we see that there is some deviation. The cut is placed at V = 165° in order to preserve as much of the highest angle peak on figure 4.5, without including events not related to this peak. This is further supported by figure 4.6.

Run number 2863 at 3570 keV shows a at $\sim$ 120°. In order investigate that behavior and also put further certainty into the cut at V = 165°, the excitation energy of that run has been plotted versus the total angle. This is seen in figure 4.6.

At this proton energy we expect the alphas at E_x = 15 480 keV and 11 040 keV according to (4.2) and (4.3). This is consistent with the two high intensity peaks on figure 4.6. From this figure, it is clear that the bump at 120° is something with a much

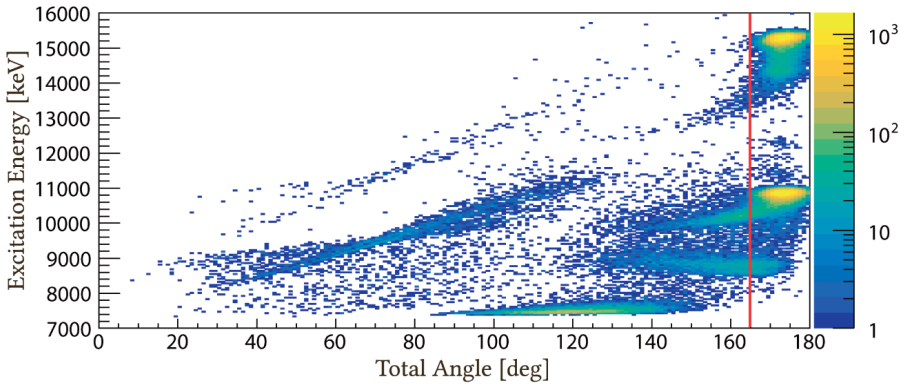

Figure 4.6: *Run 2863 from figure 4.5 plotted as a 2D histogram with excitation energy now added. The two alpha peaks are clearly visible and the cut at 165 is consistent with figure 4.5.*

lower energy than the alpha events and therefore not of interest to our analysis and something we want to cut away. The red line indicates the 165° cut and we confirm that this cut does not affect the two strong alpha peaks. We notice that each peak has a small shoulder at energies just below the predicted positions of the alpha events. This is also slightly visible on figure on 4.4 and this shoulder will be discussed in greater detail when it becomes more evident.

Our second cut will be related to the time between detections of the alpha, TA, and the carbon, TC. On figure 4.7, the absolute value of TC-TA has been plotted for the same three sample runs as the figures above.

We see that the most common time difference between these detections is close to 10 ns, while the majority happens within 30 to 35 ns. It is possible to narrow these cuts even further though. In figure 4.8, the excitation energy has been plotted against the absolute value of TC-TA for run 2863.

Again, the alphas are easy to distinguish and we see that we may place cuts as low as a value of −10 ns for TC - TA and either 20 ns or 40 ns depending on which alpha channel we are gating on.

Figure 4.9 and 4.10 contain plots similar to the last four plots describing the angular and time dependent cuts, although these are applied to the total momentum in the center-of-mass. Here the cuts are established to be at 50.

The three cuts discussed above have been gathered in table 4.2.

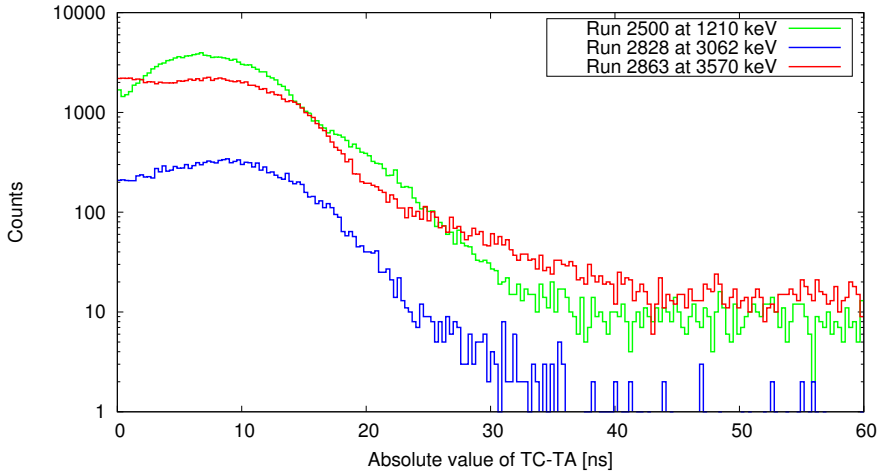

Figure 4.7: *Histrogram of |TC-TA| for three different runs, 2500, 2828 and 2863.*

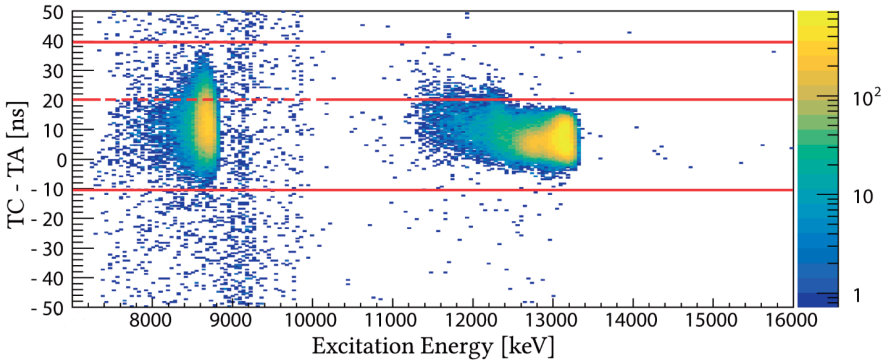

Figure 4.8: *2D histogram of TC-TA vs excitation energy. This has only been plotted for run 2863. Again we clearly see the two peaks and cuts are selected based on those and are labeled with the red lines.*

Table 4.2: *Table of the different cuts chosen for distinguishing α_0 and α_1 events from the background.*

	V [deg]	TC - TA [ns]	dP.Mag []
Cuts on α_0	> 165	> -10, < 20	< 50
Cuts on α_1	> 165	> -10, < 40	< 50

These cuts have been applied to the plot of excitation energy from figure 4.4 and the difference can be seen in figure 4.11.

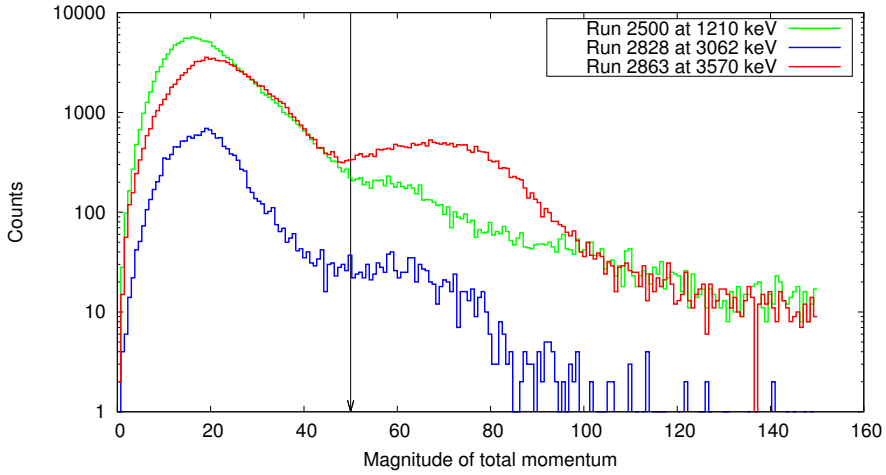

Figure 4.9: *Histogram of total momentum for runs 2500, 2828 and 2863. A preliminary cut is placed and labeled by the black arrow.*

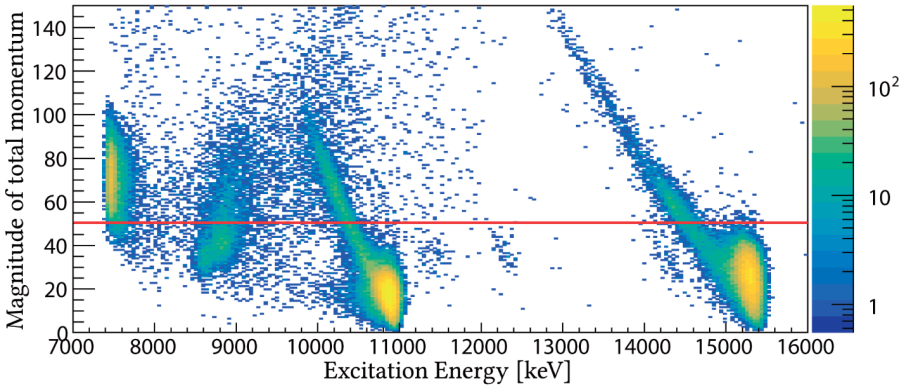

Figure 4.10: *2D histogram of total momentum vs excitation energy. This has only been plotted for run 2863. Cuts are selected and are labeled with the by the red line.*

From the blue line it is evident that we now have two well defined peaks, one containing α_0 and the other α_1. The highest of the two, the α_0 peak looks to have a pretty definitive shoulder as mentioned earlier. The cause of this has not been identified. It appears to be good events with normal behavior, but shifted a few hundred keV down from the rest. A slightly more stringent cut on momentum is able to eliminate these events, but the events contained within the shoulder seems to be α_0 events, meaning that cutting them is not desirable. It may be an effect of the

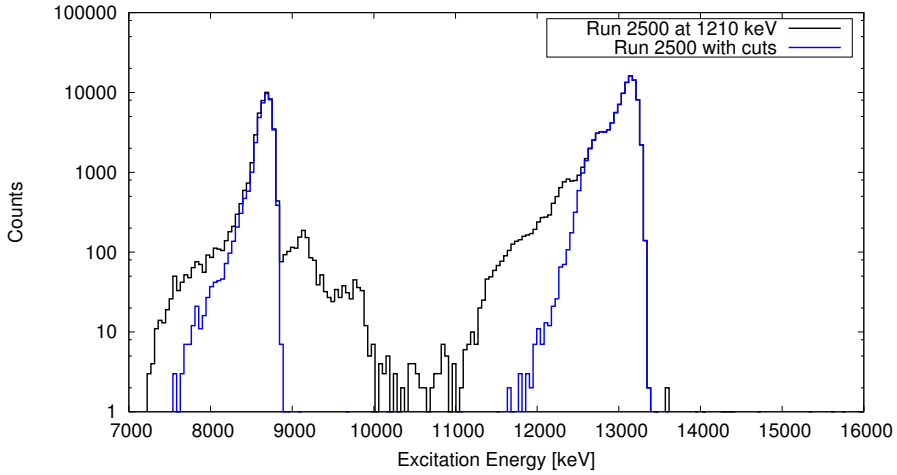

Figure 4.11: *The histogram from figure 4.4 (black histogram) with cuts applied in the blue histogram. The two alpha peaks are now clearly distinguishable.*

grid of contacts on top of the W detectors, which covers 2 % of the detector surface. This fits with the magnitude at which the shoulder starts and it can be shown that they are only present in the W detectors.

To obtain the yields of α_0 and α_1 one must now integrate each of the two peaks. This will need to be corrected for dead time in the detector readout and also be scaled with integrated beam current, to allow for comparison of yields from different runs at different beam intensities, energies and run duration. The dead time values are stored in the unpacked files and the integrated current can be calculated from the matched files. A value for integrated current, IC and dead time, DT, has been determined for every run number along with the yield of α_0 and α_1. In order to calculate the cross section the detection efficiency must be estimated for the two setups used for the two experiments. The difference in solid angle changes quite significantly from the different detector setups in IFA022 and IFA028, so efficiencies must be calculated separately for each setup.

4.3 Simulations of Efficiency in α_0 and α_1 detection

Since the detection system used for the IFA022 and IFA028 experiments does not offer full 360° detection, some particles will inevitably exit without being detected.

To gauge the extent of this, a series of simulations of the ^{15}N(p,α_x)^{12}C reaction were performed using simX. The results of these can be seen in figure 4.12.

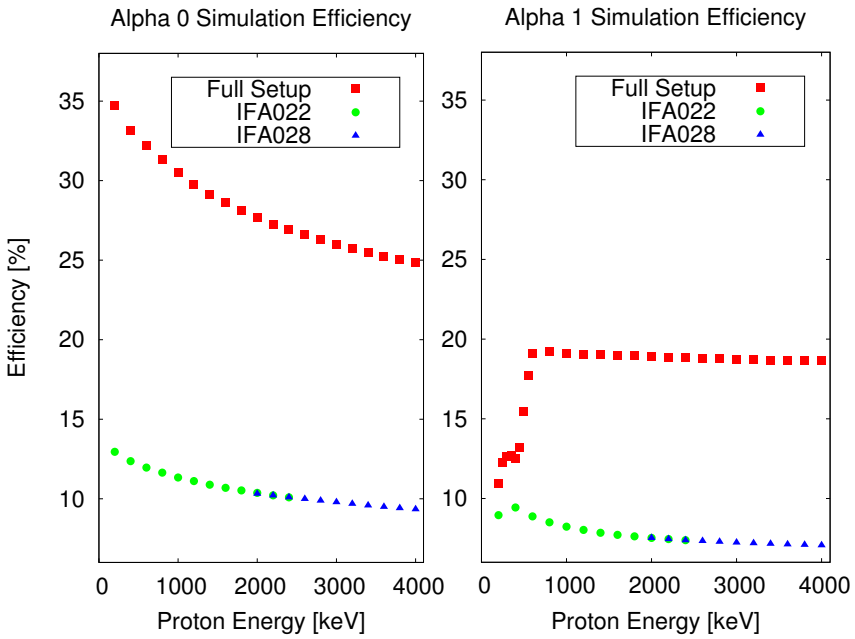

Figure 4.12: *Detection efficiency of α_0 and α_1 at energies from 200 to 4000 keV. using both the full detection setup and those implemented for the IFA022 and IFA028 experiments.*

Simulations were performed using 10^5 incoming particles and efficiencies were calculated as the number of detected particles divided by the number of incoming particles. Simulations of both the α_0 and α_1 reactions can be found on the left and right sides of figure 4.12 respectively. The red squares are simulations performed using the full detection setup, meaning that all strips are active on all four detectors. The green circles represent simulations using the setup from the IFA022 experiment and the blue triangles represent the setup from IFA028. A simulation was performed every 50 keV, but only plotted every 200 keV since the resolution was sufficient. At the lower end of the α_1 simulation with the full detection setup, simulations at every 50 keV are included to better represent the rapid rise of the detector efficiency. This rapid rise in α_1 counts at low energy, is explained by the alphas at this proton energy not having enough energy to effectively make it to the detector without getting

stopped in the dead layer or the target. It is worth noting that a small overlap was simulated between the IFA022 setup and the IFA028 setup, and they seem to have no discernible difference in efficiency, despite the difference in solid angles.

Simulations of the full detection setup versus the ones used in IFA022 and IFA028, show that the disabling of strips as discussed in section 4.1 has had a large impact on the efficiency of both α_0 and α_1 detections. Detections of α_0 decline from 35 % at 200 keV to 13 %. At 4000 keV the efficiency falls from 25 % to 10 %. This is mirrored in the α_1 detections, where efficiencies roughly decline 10 % over the full range of energies. In α_0 this corresponds to a ~ 60 % decrease in yield and this is mirrored in the α_1 yields. This however is still well within the range of detection and as we have seen earlier, there is sufficient statistics on both alpha-channels. Now that values for dead time, integrated current, efficiency and yields of α_0 and α_1 have been obtained, they can be combined into cross sections.

4.4 Cross Sections of α_0 and α_1

From equation (1.5) in section 1.3 it is given that the cross section of a nuclear reaction will be described by,

$$\sigma = \frac{q \cdot e}{IC} \cdot \frac{m}{\rho \Delta t N_a} \cdot \frac{N}{DT \cdot \epsilon}.$$

where N is the reaction yield, IC is the integrated current, DT is the dead time of the detector readout and ϵ is the detector efficiency of the setup. In the previous section we have determined yields of α_0 and α_1 along with simulations of the detector setup efficiencies used in the different IFA experiments. Values for IC and DT are available through the data files and the remaining values that go into (1.5) are parameters that do not change from run to run. With this we can calculate cross sections as a function of energy. Performing these calculations, indicates that all runs performed in March of the IFA028 experiment share a shift in energy of ~ 30 keV compared to the rest of the IFA028 runs. This includes run numbers from 2758 to 2799. All runs taken after March are consistent with each other. This shift can be seen in figure 4.13, where the IFA028 special setup has been split into IFA028 special (March) and IFA028 special (April).

No overlap between IFA022 and IFA028 is available and one could just as well argue that runs from March has the correct energy as those from April having the

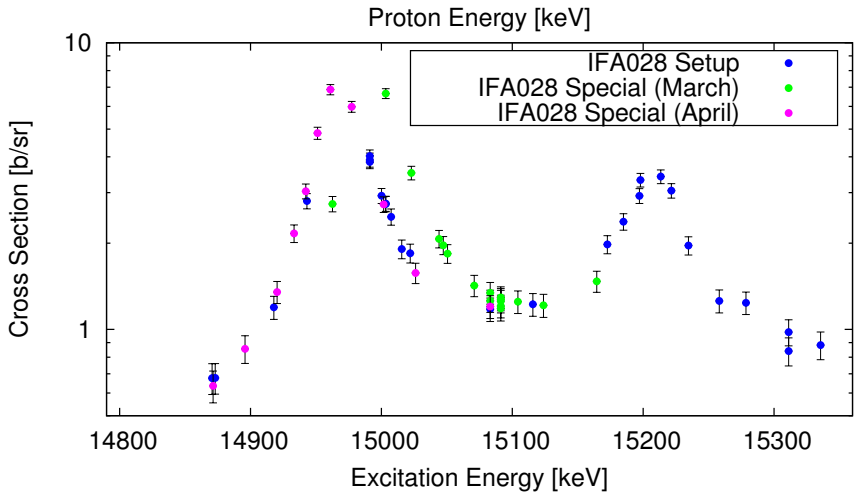

Figure 4.13: *Cross sections of the α_1 reaction as a function of energy. Data from March (green points) display a different energy distribution than the remaining data points. Shifting the energy of these points down* 30 keV *fixes the discrepancy.*

right energy. The reason for this shift is not known at present.

In figures 4.14 and 4.15 data from all 214 runs have been plotted. All data from March has been shifted -30 keV in proton energy to be consistent with the majority of the runs. We will discuss why the -30 keV shift was chosen shortly, but arguments could be made for both at this moment. Larger versions of figures 4.14 and 4.15 are available in appendix E and F.

As the yield is Poisson distributed its error are based on the square root of counts and a 5 % error in the thickness of the target. Errors in the energy calibration should be less than the size of a data point in the figure. Note that the target is turned 45° in relation to the beam, so target thickness is effectively slightly thicker than what was presented in section 2.3.

These two figures are the culmination of all 214 runs, merged into one continuous scan. The data has been split into four different categories due to the additional problems with the IFA028 data. Everything from the IFA022 experiment is gathered in one setup and is plotted as the red points on both figures. Data from IFA028 was

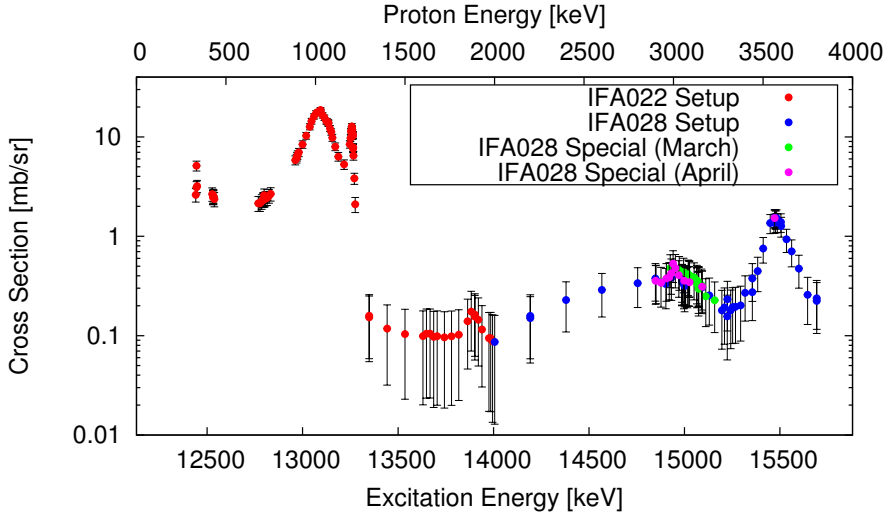

Figure 4.14: *The completed energy scan in the α_0 channel plotted as cross sections as a function of energy. The data is split into different setups that have been discussed earlier.*

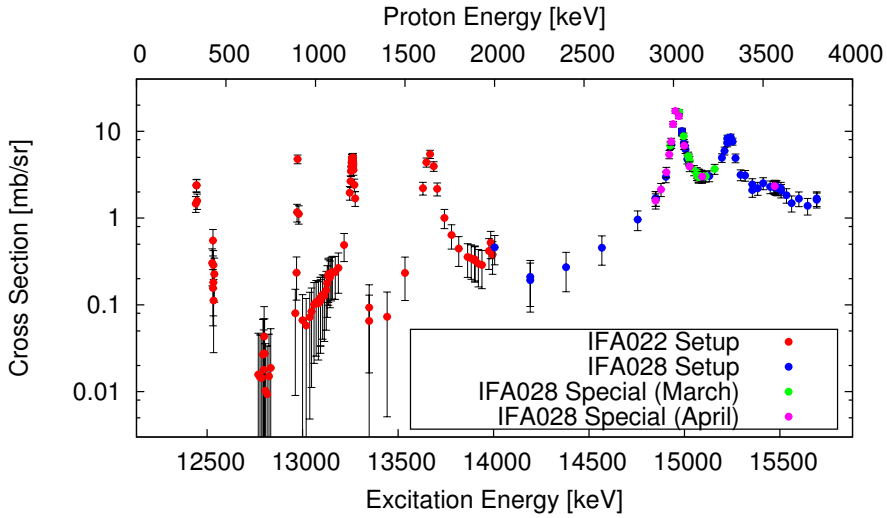

Figure 4.15: *The completed energy scan in the α_1 channel plotted as cross sections as a function of energy. The data is split into different setups that have been discussed earlier.*

earlier split into the IFA028 setup and IFA028 special setup.

The magnitude of cross sections throughout the scan appear consistent with liter-

ature, even though comparisons proved hard to achieve. In 2013, ref. [3] finds values for the cross section of the 1028 and 1210 keV resonances in α_0 to be somewhere in between 10 to 50 mb/sr. Values are read from a logarithmic plot in FIG. 8. in [3] and therefore somewhat hard to precisely estimate. Maximum values of the runs related to those peaks in figure 4.14 are 12 and 18 mb/sr respectively, which compares well with the values from 2013.

In order to get a more precise estimate of the centroid energy and width of the peaks in figures 4.14 and 4.15, they have all been fitted to the Breit-Wigner formula from equation 1.6,

$$\sigma = \frac{\pi}{k^2}(2l+1)\frac{\Gamma^2}{(E_s - E)^2 + \Gamma^2/4}$$

This will provide a centroid energy E_s and a width Γ for each of the resonances. Note that this formula should only be used on isolated resonances with no influences from neighboring levels, meaning that this method used to obtain E_s and Γ is flawed and results should be taken as a first approximation. Precise estimates of E_s and Γ will only be obtainable with more advanced methods such as an R-matrix fit.

The values of E_s and Γ from these fits are available in table 4.3. Fits have only been performed where data for fitting was sufficient and the area resembled a single isolated peak.

Table 4.3: *Left: Proposed states of ^{16}O at these proton energies, with J^π and width Γ_{lab}. Literature is based on [8]. Middle and right: Fits of centroid energy E_s and width to equation* (1.5) *to the α_0 and α_1 data from figures 4.14 and 4.15.*

Litterature			a_0 channel		a_1 channel	
E_p [keV]	Γ_{lab}	J^π	E_s [keV]	Γ [keV]	E_s [keV]	Γ [keV]
335 ± 4	110 ± 4	1^-	-	-	-	-
430 ± 0.09	0.1 ± 0.01	2^-	-	-	-	-
710 ± 7	40 ± 40	0^-	-	-	-	-
897 ± 0.29	1.47 ± 0.04	2^-	-	-	903 ± 0.1	4 ± 1
1028 ± 10	140 ± 10	1^-	1023 ± 3[a]	164 ± 5[a]	-	-
1050 ± 150	-	2^+	1077 ± 4[a]	23 ± 24[a]	-	-
1210 ± 3	22.5 ± 1	3^-	1207 ± 0.3[a]	20 ± 1[a]	1207 ± 0.1	25 ± 1
1640 ± 3	68 ± 3	1^+	-	-	1640 ± 1	69 ± 4
1890 ± 20	90 ± 2		1882 ± 4	150 ± 20	-	-
1979 ± 3	23 ± 2	2^-	-	-	-	-
2982 ± 6	55 ± 5	2^+	2991 ± 16	?[b]	3021 ± 1	54 ± 2
3170	330 ± 100	0^+	-	-	-	-
3264 ± 11	67 ± 4	2^-	-	-	-	-
3340	315 ± 100	2^+	-	-	3314 ± 2	59 ± 9
3499 ± 8	131 ± 18	3^-	3578 ± 2	151 ± 6	-	-

[a] From sum fit to three Breit-Wigner peaks.

[b] Width cannot be accurately resolved from the statistics

Starting from the lowest energy states and comparing table 4.3 with figures 4.14 and 4.15. Here we see that the lowest four states are not identified in the fits to the α_0 scan, and only the most energetic of the four is identified in α_1. The 0^- and two 2^- states are not resonant in α_0, so these were never expected to be visible in the scan. The 1^- state at 335 keV should be very obvious though, with a partial width of Γ_{α_0} = 102 keV [8]. From the scan we see that it has a large cross section compared to what is around it, but we do not have the statistics to resolve the peak. Only four runs

were carried out at this energy, one at 331 keV two at 335 keV and one at 339 keV. Expecting to be able to fit the peak from that would be very optimistic. Data in the low energy range is very sparse due to the difficulty in tuning the beam at such low energies. We do however note that this state is present in both reaction channels, even though no fits can be performed. The 2^- state at 897 keV is very obvious in the α_1 channel, at E_s = 903 keV. This state supposedly has a very narrow width of 1.47 keV and the fit also shows a narrow width of 4±1 keV. Since estimates of error in the fits are only based on the covariance matrix of the fit, narrow peaks will have very well defined values of E_s.

The energy range from ∼ 1000 to 1300 keV has three levels in close proximity to each other. All three are resonant in the α_0 channel and the same is likely true for α_1, but only the 3^- state at 1210 keV can be resolved with a fit. A fit to a sum of three Breit-Wigner resonances was performed to the α_0 scan. This was done in an attempt to resolve the state on the right side of the broad 1^- state. This state is not very well understood and any information on it is of great interest. The results of this can be seen in figure 4.16.

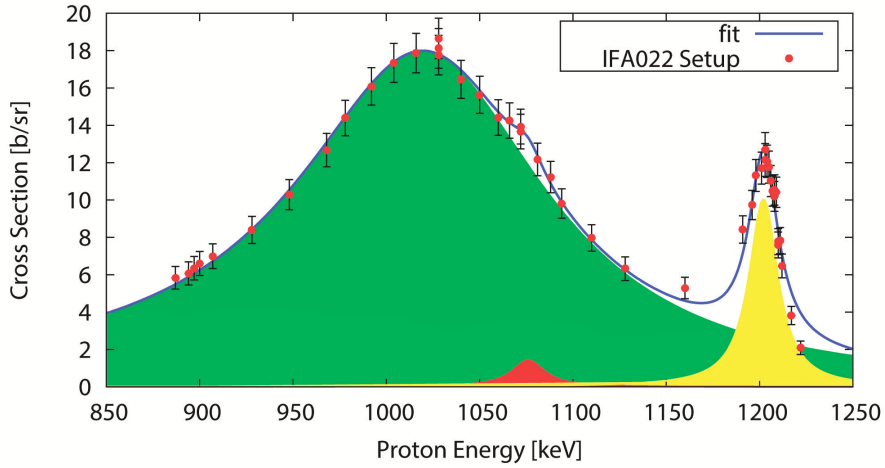

Figure 4.16: *A fit of the sum of three Breit-Wigner peaks to the α_0 cross sections data in the range of 850 to 1250 keV. Data is plotted along with the fit and each peak is illustrated by a shaded color area.*

Here the three resonant contributions have been shaded in different colors and plotted below the fit and data points. We see that this fit is very successful in following

the shape of the data points, and we get very close to the E_s values of all states. The 2^+ state on the shoulder is estimated to be at 1077 ± 4 keV, with the uncertainty based only on the covariance matrix of the fit. This is within the range proposed in the literature, $E_s = 1050 \pm 150$ keV and the values for the states on either side of that, are also within the uncertainties of the literature. This is very impressive when considering the somewhat flawed method used to obtain it. We see that this fit does not quite fit the behavior of the data on the left of the narrow 3^- state. This width of the broad 1^- is also slightly to broad when compared to the literature. However, it might be possible to resolve these issues with a more advanced analysis. At 335 keV another strong 1^- state is present. These two 1^- states would interfere, leading to either constructive or destructive interference between them, with the opposite effects on the left and right side of that. Assuming these interfere constructively in the area between them, this would pull the left edge of the resonance at 1028 keV towards lower energies. Making the width appear slightly wider and the centroid appear at a lower energy. The destructive interference on the right side of the peaks, could then be responsible for pulling the right side of the 1210 keV peak lower, than what we see from the Breit-Wigner fits. These effects would all be included if an R-matrix fit was performed. This motivated the extraction of the angular distributions, which will be covered in chapter 5, which will then hopefully provide the basis for an R-matrix analysis of the entire scan at a later time.

Only the 3^- of these three states, was possible to fit in the α_1 scan. The centroids of this state in α_0 and α_1 are fitted to the same value of 1207 keV, which is within the uncertainty of the literature. The widths are also fitted to be similar and they are comparable to the value from the literature. The two lower energy states should also be resonant in the α_1 channel, but both have very small partial widths and the majority of the reactions will favor the α_0 channel. This makes both states unresolvable from the background.

The state at 1640 keV is not resonant in the α_0 channel, but it is very strong in the α_1 channel. The state is quite isolated from other states and very good results are obtained with the Breit-Wigner fits. The state is found at the exact value given by the literature and the width is very much the same as well. This shows the power of the Breit-Wigner fits when used in isolation. As mentioned briefly in chapter 1, this state was estimated to be a 0^+ state in 2007 [12], and proposed as a good candidate

for the four alpha cluster state in [11]. However, with this spin parity assignment it is expected to strongly couple to the a_0 channel. This is not the case in the present measurement. Once fits to the angular distributions of this state are obtained, these will provide more information on the spin parity of this state.

The two states at 1890 and 1979 keV are not clear in any of the two channels. The least energetic one is resolvable by a fit in α_0, but here nothing is seen in α_1. The most energetic state is not seen in α_0 but indications of it are present in α_1, though not enough to perform a successful fit. This is a 2^- state and hence we do not expect it to be resonant in α_0. The spin parity of the lower state is unknown, but seeing as it is not present in α_0, some values can be excluded. The spin parity might be obtainable through the shape of the angular distribution of the state. We see no indications of the 0^+ four alpha candidate proposed at E_x = 14.03 MeV, corresponding to a proton energy of 2029 keV.

No states are seen between the 1979 keV state and $\sim$ 3000 keV. Above this five states are proposed. They are located at 2982, 3170, 3264, 3340 and 3499 keV. All five should be seen through the α_1 channel and all but the 2^- state at 3264 keV through α_0. This area is slightly more problematic than the lower energy area. This is in part due to the uncertainty regarding this 30 keV shift, but also due to the massive widths of two of these states. The 0^+ state at 3170 keV has a proposed width of Γ = 330 keV and the 2^+ state at 3340 keV has Γ = 330 keV. These states will greatly overlap and boost the cross section of all the three remaining states. In α_0 we see a state very strongly peaked at 3578 keV with a large width of 151 keV, we do not see this in α_1. This must be the proposed 3^- state at 3499 keV, since this state has a large partial width of Γ_{α_0} = 103 keV, whereas the partial width of α_1 is only 1 keV. This makes the α_0 channel dominant and we do not see the contribution in the α_1 channel. The position at which we find this state is off from what is given by the literature, but the width is fairly close, though also slightly larger. It is not possible to accurately resolve any of the lower three states. IFA028 data from April does suggests something that peaks at 2991 $\pm$ 16 keV which is consistent with the 2^+state. The uneven and noisy statistics in that area makes it impossible to gauge a width of the state.

In the α_1 channel we see two distinct peaks. These are centered at 3021 keV and 3314 keV and this is with the -30 keV shift of the March data in effect, the same was

true for the two states in the α_0 channel. As discussed earlier this shift might as well be +30 keV to the April data. This would put one of these two peaks at 3344 keV, which can be seen by the green data points on figure **??** in appendix G. This lines up very closely with the 2^+ state at 3340 keV but the predicted width of 59 keV is way off from the literature value of 315 keV. This would also pull the less energetic of the two peaks up to 3050 keV an area where no state is known to reside.

This area above $\sim$ 3000 keV proves extremely hard to fit using the Breit-Wigner formalism, but since this should only be applicable in areas with isolated peaks, we cannot possibly expect to fit this to states in an $\sim$ 500 keV area containing five states, two of which have widths exceeding 300 keV. In order to resolve these states, more advanced analysis is required.

4.5 Simulations of the 4-α Breakup

We have briefly discussed the four alpha breakup in section 1.2. The following will be dedicated to exploring this phenomenon in more detail.

We listed several candidates for this cluster state but we will focus on the state at 15.10 MeV. This state corresponds to a proton energy of 3170 keV and is thus part of the IFA028 experiment. Two long runs, with the longest being run 2807 at 18 hours were performed close to this energy. These runs might also reveal something about the possible gamma transitions, as this is a very interesting state. This will be discussed in the upcoming section.

To begin with we will produce a series of simulations at different proton energies relevant to this breakup and look at the efficiency of detecting the breakup using the setup employed in the IFA028 experiment. If this proves feasible, we will explore the data from the IFA028 experiment and see if alphas matching the characteristics of the four alpha breakup have been detected. The simulation is quite simple. As earlier, we feed the simulation the setup and a simulation file. The simulation we aim to perform looks like this:

```
beam: p
target: N15
-> {
        Be8
        -> {
                a
                a
        }
        Be8
        -> {
                a
                a
        }
}
```

We see that we have a beam of protons hitting a target of ^{15}N. After the collision the compound nucleus splits into two ^{8}Be that quickly decay into two alphas. ^{8}Be has a half-life of $T_{1/2} = 6.7 \cdot 10^{-17}$ s [29], so the decay to two alphas will happen before it impacts the detectors. It will be impossible to detect the alphas right at the breakup threshold, since they would have zero kinetic energy. We choose to perform the first simulation at a proton energy of 3000 keV, well above the breakup and also below the 0^+ candidate state at 3170 keV. This simulation is carried out using the full detector setup, no detectors or individual strips turned off and a value of 10^5 protons hitting the target. The simulation is run though the Sorter but not though any further analysis. The FE branch of this simulation is plotted in figure 4.17 (top).

From the simulation we see that something does indeed get detected. The black line on figure 4.17 represents all events. The red line has a multiplicity condition that only allows multiplicity 2 and higher and likewise the blue line only allows multiplicity 3 or higher. No multiplicity 4 events were detected. The majority of triggers happen at very low energies, with almost no hits exceeding 300 keV. Energies lower than 100 keV will be cut off by the Sorter. Since we are still relatively close

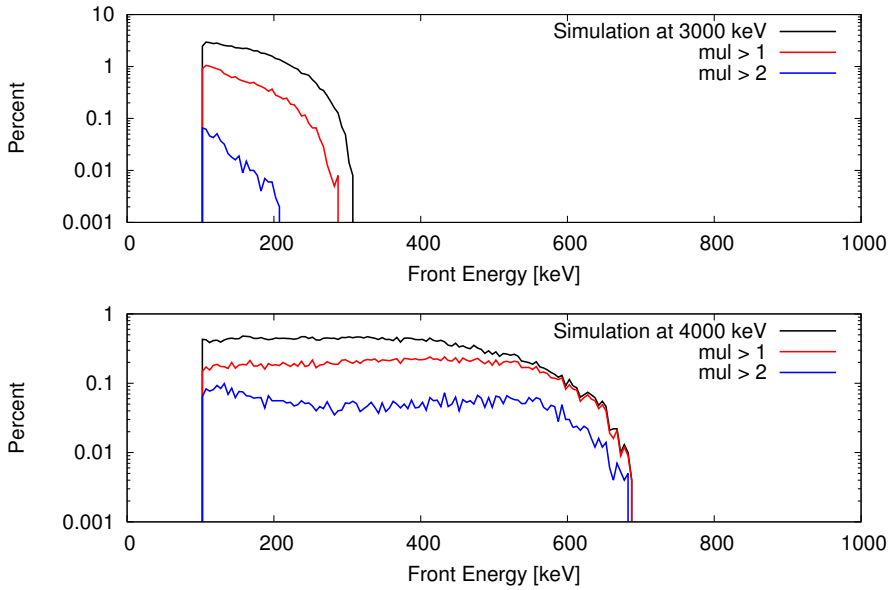

Figure 4.17: *Simulation of the four alpha breakup at a proton energy of 3000 (top) and 4000 keV (bottom). Black line represent all events, red demands multiplicity 2 or more and blue is multiplicity 3 or more.*

to the four alpha threshold and the reaction does not have a positive Q-value, we cannot expect to get high energy alphas. This can be improved by moving to higher energies.

The simulation can easily be repeated for higher energies and this will allow us to inspect how the detection rates changes with energy. The energy range of the simulation was expanded to a maximum value of 4000 keV, since we cannot reasonably expect to produce beam energies larger than that at the Aarhus facility. A plot of the simulated events at 4000 keV can be seen on figure 4.17 as well (bottom). A run was simulated every 100 keV and the number of detected events at these energies can be seen in table 4.4.

The simulation data from tabel 4.4 can been recalculated to efficiencies, simply by dividing the number of simulated events by detected events. The simulation was kept constant at 10^5 simulated events per energy range and the resulting efficiencies have been plotted and can be seen in figure 4.18. In this figure multiplicity 1 events were omitted, due to the lack of information provided by these kinds of events.

Table 4.4: *Recorded number of events in a simulation of four alpha breakup at proton energies from* 3000 *to* 4000 keV*. Data from the simulation at* 3000 *and* 4000 keV *is also represented in figure 4.17.*

E [keV]	Mul > 0	Mul > 1	Mul > 2	Mul > 3
3000	51456	7387	164	0
3100	58408	13087	834	0
3200	63296	13087	1901	2
3300	67119	17817	2989	23
3400	70492	21548	3991	104
3500	73105	24788	4886	249
3600	75139	27780	5917	426
3700	76367	30661	7038	635
3800	76918	33455	8222	872
3900	77113	35735	9360	1095
4000	77057	37518	10370	1298

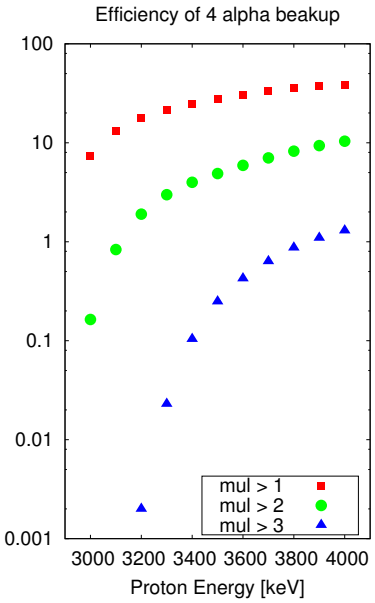

Figure 4.18: *Detection efficiency of the four alpha breakup at different energies and multiplicities.*

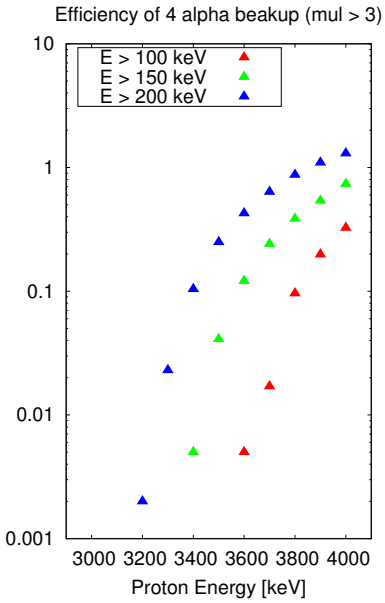

Figure 4.19: *Detection efficiency of the four alpha breakup with multiplicity 4 with different energy cuts.*

From this figure it is very clear that detection efficiencies will never be very good. At 4000 keV the detection efficiency peaks at 1.3 % for multiplicity 4. Multiplicity 3

and above has an efficiency of 10.4 % at 4000 keV and multiplicity 2 and up makes it to almost 40 %. This is still rather significant, considering the small detector efficiency in this setup.

In figure 4.19 an additional constraint is included, namely an energy cut. The blue triangles are equal to what was seen in figure 4.18 with a lower energy cut of 100 keV, that is enforced by the Sorter. The green and red triangles illustrate lower limits of 150 and 200 keV respectively. With the condition of at least 200 keV for each alpha, the detection rate at multiplicity 4 drops to 0.3 %. For multiplicity 3 and above, the efficiency falls to 3.5 %.

So far all simulations have been carried out with all strips on all detectors active. If we change this to reflect the detector setup utilized in the IFA028 experiment, where most if not all of SD was disabled, the outermost strips on the W's and the none functional spokes on SU, detection efficiencies fall to none-existing levels for multiplicity 4. These values have been included in table 4.5. A comparison between full detector activation and the setup from the IFA028 experiment is available in figure 4.20. With this in mind, it will be very hard to detect anything higher than multiplicity 2 at energies below 3500 keV.

Table 4.5: *Recorded number of events in a simulation of four alpha breakup at proton energies from* 3000 *to* 4000 keV. *This table differs from 4.4 in that it uses the detector setup from the IFA028 experiment.*

E [keV]	Mul > 0	Mul > 1	Mul > 2	Mul > 3
3000	14942	1418	0	0
3100	18373	2240	0	0
3200	20730	3125	0	0
3300	22647	3978	2	0
3400	24037	4851	26	0
3500	25065	5745	128	0
3600	25883	6601	275	0
3700	26565	7360	556	2
3800	27017	8003	933	5
3900	27213	8513	1373	11
4000	27468	9037	1900	19

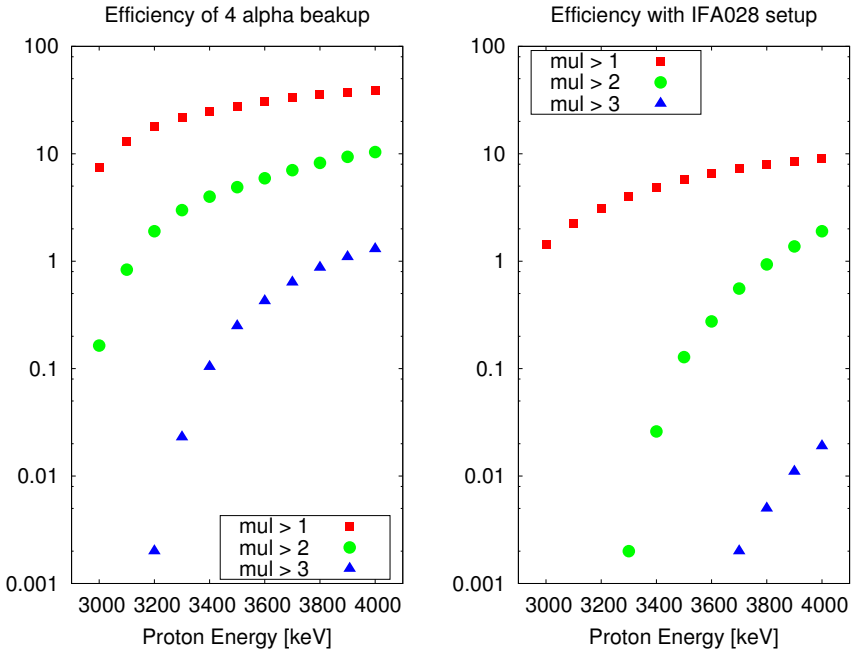

Figure 4.20: *Comparison of detection efficiency of the four alpha breakup at different energies and multiplicities. On the left all detectors are active, on the right the setup from the IFA028 experiment is active.*

Searching for the 4-α Breakup in the data

A good candidate for the four alpha cluster state is as mentioned the 0^+ state at E_x = 15.1 MeV [30][31]. This state is available experimentally at a proton energy of 3170 keV. During the IFA028 experiment, an 18 hour run, run 2807, was performed at a proton energy of 3160 keV. This is slightly below the resonance, but the state has a proposed width of 330$\pm$100 keV [8]. 3160 keV is still well within the peak of the resonance, but considering the resonance is so wide and the detection efficiency of the 4 alphas is very energy dependent, moving up a few hundred keV would still allow us to probe the resonance, while providing more available energy for the alphas. This is something that should be considered in future studies of the 4 alpha breakup.

In order to search for high multiplicity events in this run, we need to establish a baseline of how likely random coincidences are. In figure 4.21 a histogram of the

event duration, that is the time from the first hit to the last hit, for multiplicities 2, 3 and 4 has been plotted.

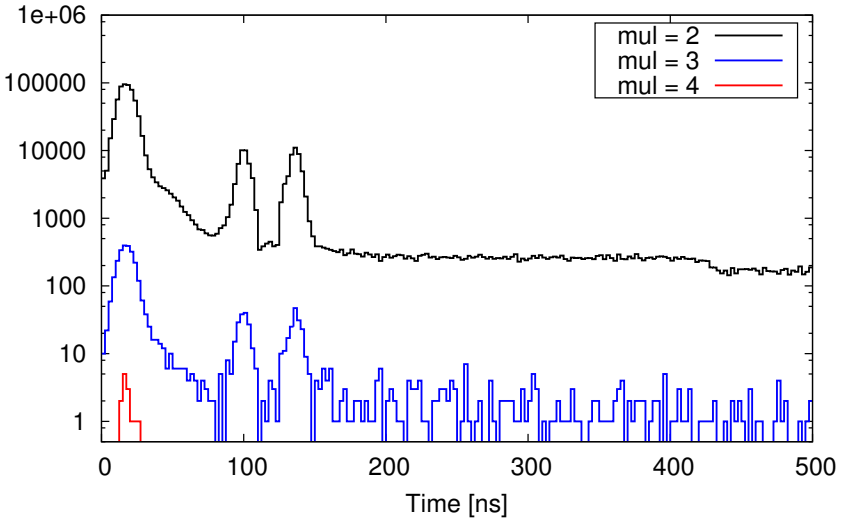

Figure 4.21: *Histogram of the event duration, that is the time from the first hit to the last hit, for multiplicity 2, 3 and 4 events in run 2807 at 3160 keV.*

We expect random coincidences to be - well, random. This would mean that a baseline of random coincidences should be present at all times. We see this in multiplicity 2 and 3 on the plot. However, multiplicity 4 events are grouped well within the accepted 100 ns window that the analyzers impose on the data. This suggests that these multiplicity 4 events are not the product of random coincidences, but real events. It should be noted that this run contains 23 million hits, and the multiplicity 4 events are made up of 52 hits. This low yield could very well allow detections of these events, even though simulations suggest it is impossible, since the simulation only performed 10^5 events. In order to investigate the multiplicity 4 events, a gate was put on these and the kinematics of the events plotted. This can be seen in figure 4.22.

The upper red curve is the kinematic curve for the α_0 reaction and the lower one is the α_1 reaction. This shows that some of the multiplicity 4 hits are consistent with

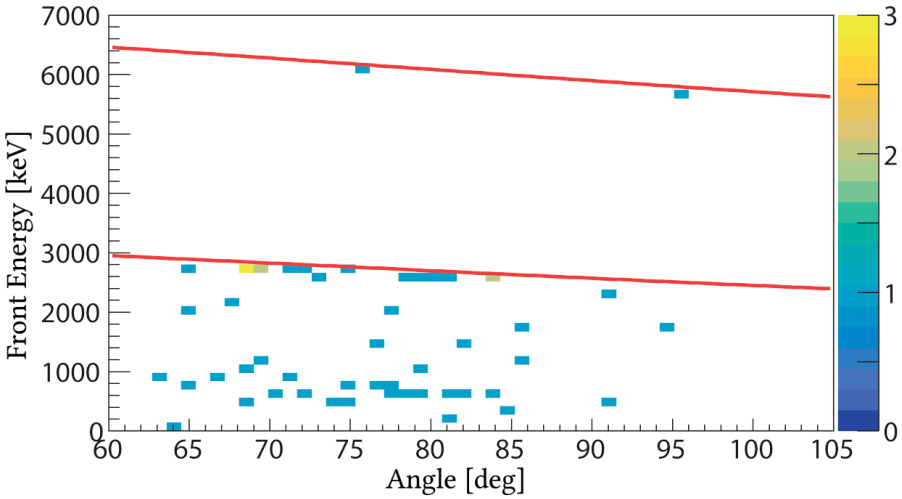

Figure 4.22: *Kinematics of multiplicity 4 events. Plotted in red are kinematic curves for the α_0 and α_1 reactions.*

the alphas we know we are producing. According to the simulations in figure 4.17 we expect the alphas from a 4 alpha breakup to have no more than 400 keV of energy, since this run was performed at a proton energy a few hundred keV above 3000 keV. Only 3 of the 52 hits are below this threshold and this seems to be definitive evidence that we do not see any signs of the 4 alpha breakup at multiplicity 4, even though the event durations were looking promising.

An alternative way of investigating the 4 alpha breakup would be to look for multiplicity 2 events with the energy of the two detected alphas matching the ground state energy of ^{8}Be. This would provide confirmation of ^{8}Be being formed and this would be enough to infer the breakup into two ^{8}Be quickly followed by the decay into 4 alphas, without ever detecting all 4 alphas. According to the simulations, detections of multiplicity 2 events should be very possible, but in order to detect the two alphas in this manner, the doubles analysis would have to be rewritten and this is beyond the scope of this thesis. This means that detections of the four alpha breakup cannot be confirmed at present. However, simulations do not predict possible detections when looking for multiplicity 4 events, and thus it would confirm that these simulations are correct. Subsequent analysis of these runs may still confirm the presence of this four alpha clusters state, but nothing is seen yet.

4.6 The Search for Gamma Transitions

We have earlier briefly discussed the possibility of detecting alphas with energies lower than what is expected from the reactions we have been analyzing so far. These lower energy alphas would be the result of the ^{16}O compound nucleus gamma transitioning into a lower lying state, before proceeding with alpha decay. Since energy would be released in the gamma decay, less energy would be available for the alpha particle. If we can detect these, we may be able to infer the locations of these lower lying states in ^{16}O and compare strengths of the alpha and gamma channels. The 1^- state at E_x = 9.59 MeV is a great candidate for this and is of great interest, since it very relevant for the astrophysical models outlined earlier.

In order to investigate this, we will once again examine run 2807 at 3160 keV. This time we begin by looking at the excitation energy of this run. This has been plotted in figure 4.23.

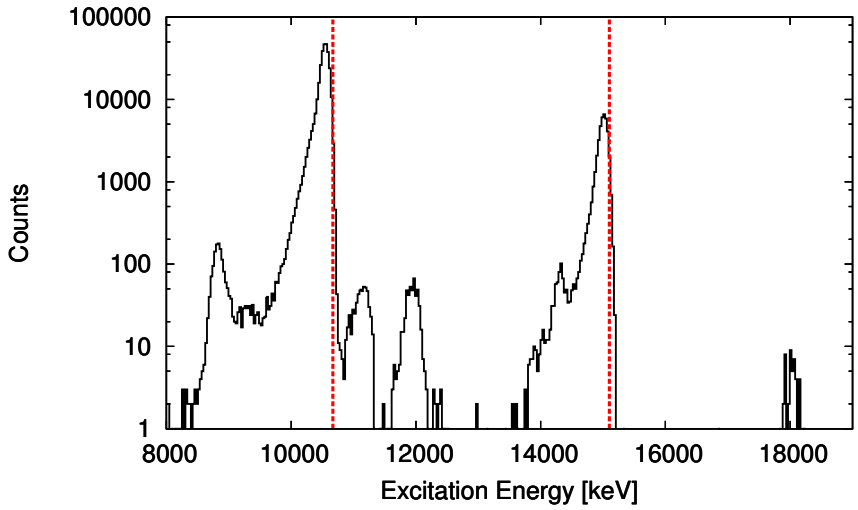

Figure 4.23: *Excitation energy histogram of run 2807 at a proton energy of 3160 keV. Marked in red dotted line are the positions of the calculated α_0 and α_1 energies. Between these two small peaks are visible, which was speculated to be the result of gamma transitions.*

The cuts from section 4.2 have been applied to the data and as expected we get a histogram closely resembling the blue line from figure 4.11. Plotted in dotted red lines are the energies at which we expect to find the α_0 and α_1 reactions. Around 9000 keV we see a peak that appears to be punch-through in the detectors. This will become more clear when we analyze the kinematics of the run. This leaves us with three unidentified peaks. One all the way up at 18 000 keV that is of little interest, since the gamma transitions are supposed to have lower energy. The remaining two at 11 000 and 12 000 keV respectively are very interesting. These could be the result of energy lost to the gamma transitions. The peak at 12 000 keV could very well be the 0^+ state in ^{16}O at E_x = 12 049 keV since the gamma transition from this to the ground state would be forbidden and only alpha decays are allowed. The lower of the two also coincides with a number of proposed states in ^{16}O located around 11 000 keV.

In order to further investigate the properties of these peaks, the kinematics of the run has been plotted in figure 4.24.

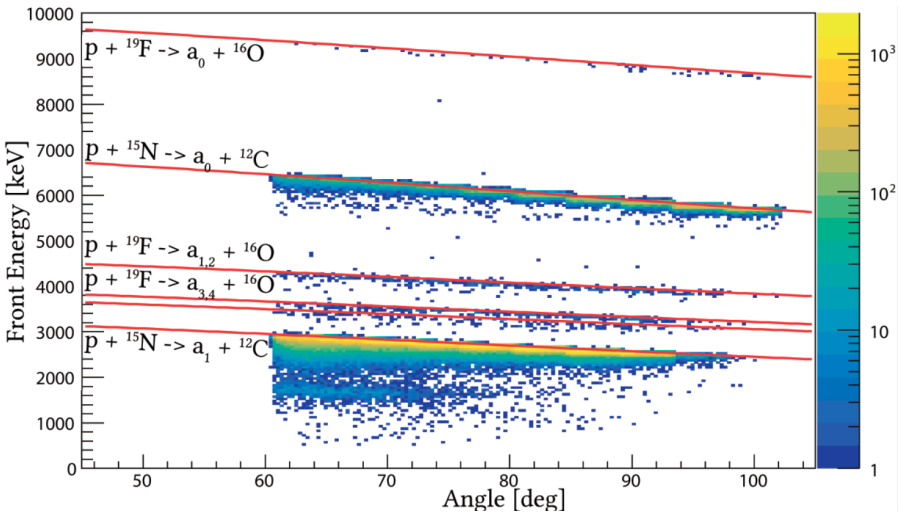

Figure 4.24: *Kinematics for the 2807 run. Kinematic curves for several different reactions are plotted in red lines. These are denoted on the left of each line.*

In figure 4.24 the kinematic curves of the α_0 and α_1 reactions are very clear as expected. Surprisingly, the three unidentified peaks have very strong agreement with the ^{19}F(p,α_x)^{16}O reactions. The peak deemed uninteresting for gamma transitions

fits very well with the α_0 reaction if we do have some amount of ^{19}F in the target. The four bound states in ^{16}O, responsible for the $\alpha_{1,2,3,4}$ reactions also fit the kinematics closely. The first two states are so close in energy that they appear as one, but the states at 6.917 and 7.117 MeV are far enough apart that they would show up as two bands on the kinematics. This is exactly what we see in run 2807 if it true ^{19}F would be present in the target, this seems far more likely than the peaks being a result of the gamma transitions.

The fabricator of the targets [23], was contacted and denied the possibility of ^{19}F in the target as a consequence of the production methods outlined in section 2.3. The argon gas used for sputtering is very pure, 99.9999 % and so are the carbon targets, 99.999 %. The nitrogen gas is only 99 % pure, but fluorine is not on the list of contaminants. This leaves the pump of the reaction chamber as possible contaminants, and it has earlier been suggested that the pump could be contaminated with ^{19}F, from using oil for the pump containing fluorine in a previous experiment. This seem very likely based on figure 4.24.

Chapter 5

Conclusion and Outlook

Within this thesis an energy scan of the level structure in ^{16}O from proton energies of 331 to 3800 keV has been performed through the ^{15}N(p,α_x)^{12}C reaction. This scan consists of 214 individual runs at different energies. The individual run energies were carefully selected to provide the best resolution possible. More data points at lower energies could have provided more information on the states below 500 keV, but at these low proton energies the beam stability becomes an issue and tuning proved very hard.

The results of the scan holds detailed information about nine different states to which Breit-Wigner fits have been conducted. Even more states have been observed, but not successfully fitted, however the information gathered in the scan, should be sufficient to extract information about these states trough an R-matrix analysis. Six of these nine observed states have centroid energies below E_p = 2000 keV and the values for E_s and Γ are all in good agreement with values from literature [8]. One state of particular interest is the state proposed at 1050 ± 150 keV. From a sum fit of three Breit-Wigner peaks, this state was found to be located at 1077 ± 4 keV with a width of 23 ± 24 keV. This fit is available in figure 4.16.

States above E_p = 2900 keV proved hard to fit using the Breit-Wigner formalism. This type of fit is only meant for isolated peaks and in this energy range two very wide states with widths exceeding 300 keV each, provided a large background. This is expected to strongly influence the behavior of the remaining states and resulted in fits that should only be taken as a first approximation. This problem should be

solvable by more advanced analysis methods, like an R-matrix fit. The program AZURE [32] provides a multilevel, multichannel R-matrix code packaged in a user-friendly interface. Contact was establish with James de Boer of the University of Notre Dame [33], and he has kindly forwarded everything needed to conduct an R-matrix analysis with AZURE. James has previously conducted a large scale R-matrix fit on ^{16}O [6], but has showed great interest in the data obtained in this thesis, which could be implemented within his analysis and provide further constraints on the level structure of ^{16}O. Since the main goal of this thesis is exactly this, in order to allow extrapolations to relevant stellar energies, this would be a very interesting path to follow! Sadly, time does not permit the pursuit of such analysis at the moment.

To perform a comprehensive R-matrix analysis, one would need to extract angular distributions for all runs within this thesis and provide them as input files for AZURE. This has been attempted using the Singles analysis. In figure 5.1 preliminary results of the angular distributions in the α_0 channel at the peak energy of each resonance constrained within the analysis, see table 4.3, has been plotted. The cross sections are plotted in arbitrary units, as they are normalized and scaled with energy to reflect the energies at which the resonance is present.

The resulting angular distributions do compare to the angular distributions from [34] and [35]. These can be seen in figure 5.2. Since all values are plotted in arbitrary units, it is rather hard to compare anything other than the shapes. Note that data from [34] and [35] is plotted as a function of center-of-mass angle, whereas the angular distributions from this thesis are a function of cosine of that angle. This means the shapes should effectively be mirrors of each other. The spin parity of a state can also be assessed from fitting to the angular distributions, but since these data are still very preliminary, accurate fits have not been attempted yet. The fits marked in red in figure 5.1 are simply lagrange polynomial fits, since they are only used to roughly estimate the shape.

Uncertainties on the angular distributions are rather large. They are very much affected by the detector setup used for the particular run and they are also hampered by the fact that SD yields no usable data for the angular distribution, effectively removing one third of the shape. It seems very evident that more time has to be put into obtaining the angular distributions, before they can be used as input for an R-matrix fit. It is also worth noting that we can only select the α_0 channel at

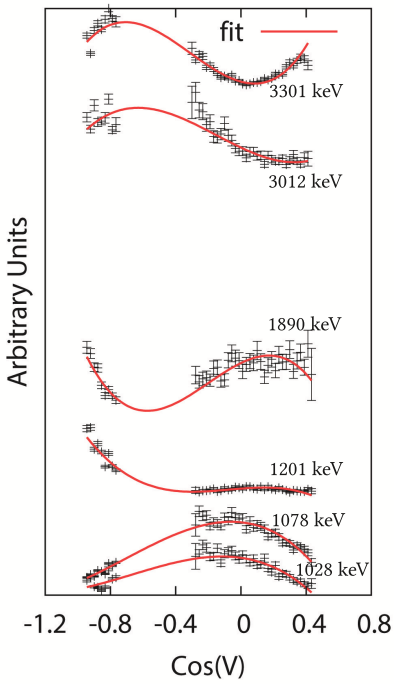

Figure 5.1: *Angular distributions at peak energies of all resonances constrained in the α_0 channel. Cross sections are plotted in arbitrary units as they are normalized and scaled with energy to reflect the energies at which the resonance is present. The numbers on the fits indicate proton energies.*

the moment, since the singles analysis allows all different kinds of events through the analysis, making it impossible to gate on the α_1 channel, since this is effectively on top of the scattered protons and the carbon nuclei of the α_0 reaction. One could attempt to rewrite the Doubles analysis code to facilitate angular distributions in the α_1 channel, but once again time constraints did not permit this.

Attempts were also made to detect the four alpha cluster state, which has been proposed to be the 0^+ state at E_p = 3170 keV. Simulations of whether these alphas would be detectable were carried out, and it is evident that the alphas would have to be detected at very low energies. At this proton energy none of the alphas would exceed 300 keV in energy. This is not something that is impossible to detect with our setup, however it would be very challenging. Simulations also show that the detection efficiency of the full multiplicity 4 events would be highly unlikely. In 10^5 simulated events at this proton energy using the IFA028 setup, not a single

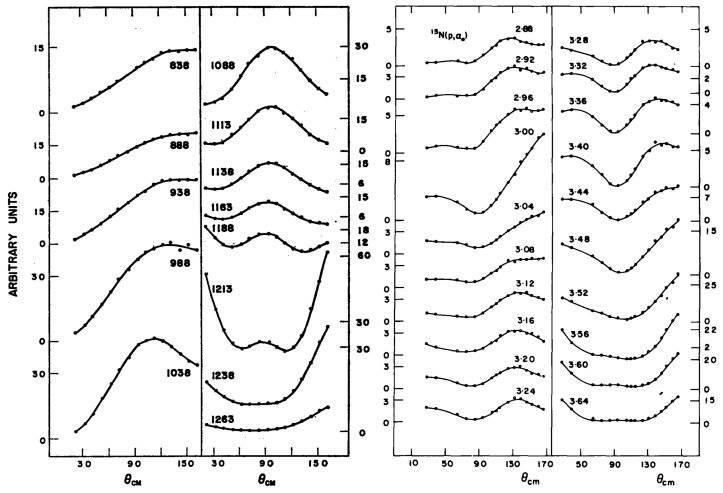

Figure 5.2: *Angular distributions from [34] and [35] in the α_0 channel. The numbers on the fits indicate proton energies.*

multiplicity 4 event was detected. For this detection to have any sort of strength, proton energies have to exceed 3600 keV. If the full setup is employed, the count rate rises to two events in 10^5 events. Clearly multiplicity 4 events will be very challenging to detect. Another way to look for this cluster state would be to look for two alphas instead of all four, since their energies would sum to the exact energy of the ground state in ^{8}Be. In order to do this, more statistics close to this energy would be needed, possibly even at higher energies. Even though that would be moving away from the peak of the resonance, the additional energy available for the alphas, might increase the detector efficiency.

Lastly, efforts were put into detecting the gamma transitions to unbound states in ^{16}O. This yielded no positive results. Contamination with ^{19}F lead to hopes that these had been seen, but all counts were likely due to the ^{19}F reactions. The strength of these could be used to put upper bounds on the partial gamma widths of the transitions.

Bibliography

[1] P. A. R Ade. “Planck 2015 results. XIII. Cosmological parameters”. In: (2015).

[2] Carlos Bertulani. “Frontiers in Nuclear Astrophysics”. In: (2016).

[3] James deBoer. “R-matrix analysis of ^{16}O compund nucleus reactions”. In: (2013).

[4] Martin Freer. “The Hoyle state in ^{12}C”. In: (2014).

[5] Kenneth Lund Andersen. “Estimating dust extinction of type Ia supernovae via V-NIR colors”. In: (2016).

[6] James deBoer. “The $^{12}\mathrm{C}(\alpha,\gamma)^{16}\mathrm{O}$ reaction and its implications for stellar helium burning”. In: (2017).

[7] Gianluca Imbriani. “Measurement of γ rays from $^{15}\mathrm{N}(p,\gamma)^{16}\mathrm{O}$ cascade and $^{15}\mathrm{N}(p,\alpha_1\gamma)^{12}\mathrm{C}$ reactions”. In: (2012).

[8] D. R. Tilley. “Energy level in light nuclei A = 16-17*”. In: (1993).

[9] kevin Ching. “Characterization of the pre-eminent 4-α cluster state candidate in ^{16}O”. In: (2015).

[10] Jonas Refsgaard. “Three-body effects in the Hoyle-state decay”. In: (2018).

[11] K. C. W. Li. “Characterization of the proposed 4-α cluster state candidate in ^{16}O”. In: (2018).

[12] T. Wakasa. “New candidate for an alpha cluster condensed state in $^{16}\mathrm{O}(\alpha,\alpha')$ at 400 MeV”. In: (2007).

[13] F. Brochard. “Etude de quelques transitions electromagnetiques dans le noyau ^{16}O”. In: (1968).

[14] Christian Iliadis. “Nuclear Physics of Stars”. In: (2007).

[15] Klaus Wille. “The Physics of Particle Accelerators”. In: (2000).

[16] Frank Daugaard. In: (2017). URL: {https://www.youtube.com/watch?v=qPVoJijzhVY}.

[17] Hans Fynbo. “Nuclear Reaction Studies at Aarhus University - the Complete Guide (in progress)”. In: (2018).

[18] Micron Semicondictor Ltd. In: (2018). URL: {www.micronsemiconductor.co.uk/product}.

[19] Olof Tengblad. “Novel thin window design for a large-area silicon strip detector”. In: (2004).

[20] Ohring, Milton. “Matrial Science og Thin Films: Deposition and Structure”. In: (2002).

[21] Sabrina Johannsen. “Upconversion of nearinfrared light through Er doped TiO2, and the effects of plasmonics and codoping with Yb”. In: (2015).

[22] Jacques Chevallier. “jach@phys.au.dk”. In: (2018).

[23] Folmer Lyckegaard. “folmer@phys.au.dk”. In: (2018).

[24] William R. Leo. “Techniques for Nuclear and Particle Physics Experiments: A How-to Approach”. In: (1994).

[25] Michael Munch. “https://git.kern.phys.au.dk/ausa/ausalib/wikis/home”. In: (2018).

[26] Michael Munch. “mm.munk@gmail.com”. In: (2018).

[27] Ilka Antcheva. “ROOT - A C++ framework for petabyte data storage, statistical analysis and visualization”. In: (2009).

[28] Michael Munch. “simX”. In: (2018). URL: https://doi.org/10.5281/zenodo.1320121.

[29] TUNL Nuclear Data evaluation. In: (2018). URL: www.tunl.duke.edu.

[30] Kiyomi Ikeda. “The Systematic Structure-Change into the Molecule-like Structures in the Self-Conjugate 4n Nuclei”. In: (1968).

[31] Kiyomi Ikeda. “Introduction to Comprehensive Nuclear Structure Study Based on Cluster Correlations and Molecular Viewpoint”. In: (1979).

[32] R. E. Azuma. “AZURE: An R-matrix code for nuclear astrophysics”. In: (2010).

[33] James deBoer. “rdeboer1@nd.edu”. In: (2018).

[34] A. D Frawley. “Levels of ^{16}O near 13 Mev excitation from ^{15} + p reactions”. In: (1977).

[35] A. D Frawley. “Levels of ^{16}O near 15 Mev excitation from ^{15} + p reactions”. In: (1977).

Appendix

A - Table of all runs from IFA022

Run:	Duration [m]	E_p [keV]	α_0 [b/sr]	Err [b/sr]	α_1 [b/sr]	Err [b/sr]
2500	91.2	1210	3.110	0.177	1.625	0.128
2502	12.0	1210	3.040	0.175	1.580	0.127
2503	12.0	1212	2.588	0.162	1.437	0.121
2504	12.0	1217	1.529	0.124	0.967	0.099
2505	12.0	1222	0.838	0.092	0.674	0.083
2506	12.1	1208	4.079	0.204	1.875	0.138
2507	12.5	1203	4.857	0.222	1.799	0.136
2508	4.5	1198	4.527	0.219	1.391	0.123
2509	56.8	1208	4.217	0.206	1.874	0.137
2510	12.0	1206	4.407	0.211	1.813	0.136
2511	32.9	1201	4.684	0.217	1.551	0.125
2512	12.0	1196	3.894	0.199	1.063	0.104
2514	13.2	1191	3.369	0.185	0.784	0.090
2515	15.0	1600	0.040	0.020	0.884	0.095
2516	15.0	1620	0.042	0.021	1.758	0.134
2517	15.6	1640	0.042	0.021	2.179	0.148
2518	15.1	1660	0.039	0.020	1.582	0.128
2519	15.0	1680	0.039	0.020	0.868	0.094
2520	12.0	710	0.941	0.098	0.007	0.009
2521	12.0	720	0.967	0.099	0.004	0.006
2522	12.0	730	0.971	0.099	0.004	0.006
2523	12.0	740	1.020	0.102	0.006	0.008
2525	12.0	750	1.068	0.104	0.008	0.009
2526	12.0	700	0.896	0.095	0.006	0.008
2527	12.0	690	0.857	0.093	0.006	0.008
2528	12.0	680	0.859	0.093	0.006	0.008
2529	12.0	887	2.335	0.154	0.032	0.018
2531	12.0	894	2.429	0.157	0.094	0.031
2532	60.0	897	2.539	0.160	0.468	0.069
2533	13.0	900	2.641	0.163	1.909	0.139

2534	12.0	907	2.797	0.168	0.447	0.067
2535	14.6	928	3.360	0.184	0.027	0.016
2537	12.0	978	5.758	0.241	0.034	0.018
2538	12.0	1028	7.248	0.271	0.048	0.022
2541	12.6	1128	2.532	0.162	0.107	0.033
2542	13.6	1060	5.768	0.241	0.059	0.024
2543	12.0	1050	6.254	0.252	0.051	0.023
2544	12.0	1040	6.585	0.258	0.052	0.023
2545	30.0	1720	0.039	0.020	0.402	0.064
2546	45.0	1760	0.039	0.020	0.255	0.051
2547	45.0	1800	0.041	0.020	0.178	0.042
2548	20.0	1850	0.056	0.024	0.143	0.038
2549	15.0	1870	0.070	0.027	0.137	0.037
2550	63.9	1890	0.062	0.025	0.130	0.036
2551	29.5	1890	0.065	0.026	0.133	0.037
2552	19.3	1910	0.058	0.024	0.119	0.035
2553	17.8	1930	0.046	0.022	0.115	0.034
2554	15.5	1969	0.038	0.019	0.167	0.041
2555	15.0	1979	0.038	0.020	0.209	0.046
2556	15.7	1989	0.035	0.019	0.152	0.040
2557	40.2	429	0.991	0.100	0.073	0.027
2559	34.1	427	1.008	0.101	0.221	0.047
2560	55.9	427	0.989	0.100	0.063	0.025
2561	38.1	431	1.004	0.101	0.045	0.021
2567	9.0	335	2.046	0.150	0.947	0.104
2569	18.1	1072	5.466	0.236	0.090	0.030
2570	10.8	1300	0.061	0.025	0.026	0.016
2571	5.9	1300	0.064	0.025	0.037	0.020
2572	8.8	1400	0.047	0.022	0.029	0.017
2573	13.8	1500	0.041	0.020	0.093	0.031
2574	12.3	1211	3.133	0.178	1.716	0.132
2575	12.0	1209	4.166	0.205	1.998	0.142
2577	13.4	1207	4.195	0.206	1.946	0.140

2578	12.0	1205	4.703	0.218	1.976	0.142
2579	12.1	1203	5.086	0.227	1.932	0.140
2580	39.1	1160	2.117	0.146	0.196	0.044
2581	10.3	1110	3.189	0.180	0.095	0.031
2582	10.1	1094	3.925	0.199	0.096	0.031
2583	10.0	1028	7.102	0.269	0.045	0.021
2584	9.5	1016	7.146	0.269	0.042	0.021
2585	11.5	1004	6.937	0.265	0.043	0.021
2586	5.0	992	6.434	0.256	0.040	0.020
2587	9.7	716	0.940	0.097	0.011	0.011
2588	9.1	713	1.036	0.102	0.017	0.013
2589	13.4	710	0.945	0.098	0.011	0.011
2590	9.8	707	0.934	0.097	0.011	0.010
2591	9.0	435	0.946	0.098	0.091	0.030
2592	9.3	429	1.025	0.102	0.115	0.034
2593	9.0	423	1.063	0.104	0.121	0.035
2594	5.0	339	1.279	0.115	0.630	0.081
2595	5.1	335	1.241	0.114	0.959	0.101
2596	6.5	331	1.045	0.104	0.587	0.078
2602	62.5	1028	7.463	0.274	0.048	0.022
2603	9.5	1066	5.703	0.240	0.071	0.027
2604	11.0	1072	5.574	0.237	0.086	0.029
2605	10.0	968	5.070	0.227	0.029	0.017
2606	11.1	948	4.115	0.204	0.023	0.015
2607	10.4	1081	4.869	0.222	0.083	0.029
2608	10.2	1088	4.491	0.213	0.093	0.031
2609	63.1	1204	4.829	0.220	1.642	0.128

B - Table of all runs from IFA028

Run:	Duration [m]	E_p [keV]	α_0 [b/sr]	Err [b/sr]	α_1 [b/sr]	Err [b/sr]
2802	46.8	3501	0.301	0.055	1.009	0.101
2804	45.3	3400	0.108	0.033	1.238	0.112
2805	45.1	3301	0.093	0.031	3.321	0.183
2806	44.2	3200	0.101	0.032	1.223	0.111
2808	6.0	3160	0.122	0.036	1.176	0.111
2809	42.9	3600	0.556	0.075	0.882	0.094
2810	36.8	3700	0.189	0.044	0.670	0.082
2811	61.9	3800	0.089	0.030	0.650	0.081
2812	64.4	3800	0.095	0.031	0.673	0.082
2815	83.2	2001	0.035	0.019	0.184	0.043
2817	83.3	2200	0.063	0.025	0.077	0.028
2818	44.6	2200	0.060	0.025	0.084	0.029
2819	53.7	2400	0.091	0.030	0.109	0.033
2820	61.4	2600	0.115	0.034	0.182	0.043
2821	51.2	2800	0.135	0.037	0.385	0.062
2822	25.2	2899	0.151	0.039	0.676	0.083
2823	44.0	2902	0.144	0.038	0.677	0.083
2824	11.6	2957	0.132	0.037	1.195	0.110
2825	6.5	2988	0.153	0.040	2.806	0.172
2827	5.2	3047	0.148	0.039	4.025	0.203
2828	23.3	3062	0.136	0.037	2.749	0.167
2829	5.9	3077	0.135	0.038	1.907	0.143
2835	4.2	3346	0.078	0.029	1.962	0.144
2836	4.8	3375	0.081	0.029	1.258	0.116
2837	3.0	3440	0.150	0.040	0.979	0.102
2838	2.5	3470	0.179	0.044	0.882	0.098
2839	3.0	3540	0.543	0.075	0.917	0.099
2840	2.1	3571	0.596	0.081	0.886	0.100
2841	2.7	3601	0.506	0.074	0.828	0.096
2842	2.2	3631	0.373	0.063	0.733	0.090

2843	2.4	3660	0.282	0.055	0.594	0.082
2844	5.2	3749	0.103	0.033	0.553	0.077
2845	1.5	3047	0.143	0.041	3.902	0.220
2846	6.9	3047	0.139	0.038	3.840	0.201
2847	9.0	3058	0.133	0.037	2.927	0.176
2848	7.5	3062	0.126	0.036	2.740	0.169
2849	11.1	3067	0.139	0.038	2.471	0.160
2850	7.3	3085	0.139	0.038	1.845	0.139
2851	7.8	3270	0.072	0.027	1.979	0.144
2852	6.4	3285	0.077	0.028	2.376	0.157
2853	6.9	3300	0.063	0.025	2.925	0.174
2854	5.1	3320	0.072	0.027	3.414	0.188
2855	5.5	3330	0.077	0.028	3.049	0.178
2856	3.1	3440	0.110	0.034	0.840	0.094
2857	2.1	3561	0.547	0.076	0.906	0.099
2858	1.4	3565	0.615	0.084	0.930	0.105
2860	2.1	3570	0.552	0.077	0.888	0.099
2861	6.2	3576	0.610	0.085	0.922	0.107
2862	1.3	3580	0.555	0.078	0.873	0.100
2863	51.6	3570	0.596	0.077	0.912	0.096

IFA028 special March

Run:	Duration [m]	E_p [keV]	α_0 [b/sr]	Err [b/sr]	α_1 [b/sr]	Err [b/sr]
2757	46.5	3140	0.118	0.036	1.183	0.114
2760	163.3	3140	0.122	0.035	1.206	0.110
2761	14.2	3140	0.136	0.037	1.254	0.114
2762	75.8	3140	0.138	0.037	1.292	0.114
2763	36.0	3140	0.138	0.037	1.274	0.114
2764	17.2	3115	0.154	0.040	1.421	0.121
2765	9.8	3090	0.162	0.041	1.836	0.138
2766	11.1	3086	0.161	0.041	1.964	0.143
2767	15.4	3082	0.166	0.041	2.067	0.145

2768	10.1	3056	0.174	0.042	3.511	0.191
2769	10.1	3032	0.182	0.043	6.643	0.263
2770	9.9	2982	0.191	0.045	2.737	0.170
2771	20.0	3130	0.144	0.038	1.340	0.117
2772	10.1	3156	0.130	0.036	1.248	0.113
2773	10.0	3180	0.100	0.032	1.212	0.112
2774	10.0	3230	0.091	0.031	1.470	0.124
2787	141.2	3130	0.134	0.037	1.257	0.112
2792	5.0	1970	0.000	0.000	0.182	0.043

IFA028 special April

Run:	Duration [m]	E_p [keV]	α_0 [b/sr]	Err [b/sr]	α_1 [b/sr]	Err [b/sr]
2866	14.3	2900	0.143	0.038	0.635	0.081
2868	6.2	2930	0.136	0.037	0.856	0.095
2869	4.7	2960	0.151	0.040	1.351	0.119
2870	3.8	2976	0.154	0.040	2.162	0.153
2871	3.6	2987	0.170	0.043	3.035	0.181
2873	2.0	3010	0.192	0.046	6.866	0.283
2874	5.0	3030	0.162	0.042	5.981	0.261
2875	3.9	3060	0.143	0.039	2.730	0.170
2877	5.7	3090	0.138	0.038	1.574	0.128
2878	2.0	2998	0.212	0.048	4.841	0.235
2879	87.2	3565	0.610	0.078	0.933	0.097
2807	1107.5	3160	0.125	0.035	1.202	0.110

C - Detector hit patterns in IFA022

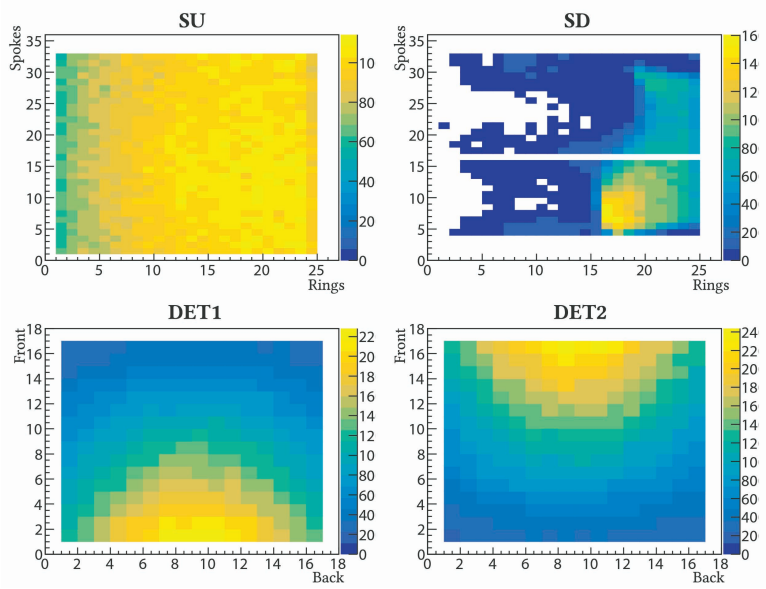

Figure 1: *Hit pattern on run 2532 from IFA022 at a beam energy of 897 keV*

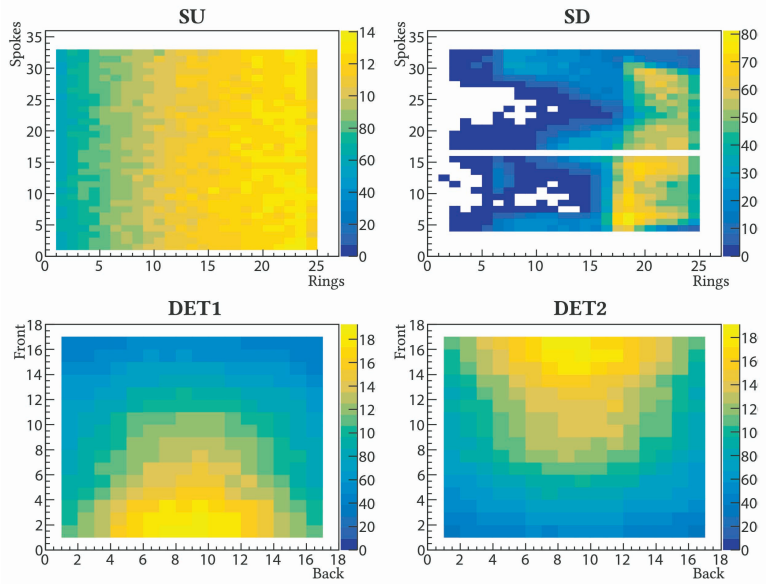

Figure 2: *Hit pattern on run 2552 from IFA022 at a beam energy of 1910 keV*

D - Detector hit patterns in IFA028

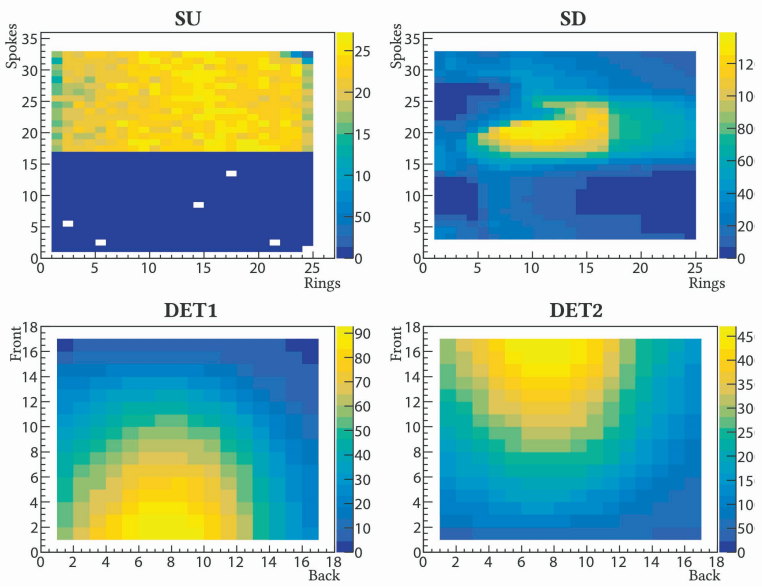

Figure 3: *Hit pattern on run 2864 from IFA028 at a beam energy of 1640 keV*

E - Full Energy Scan in α_0

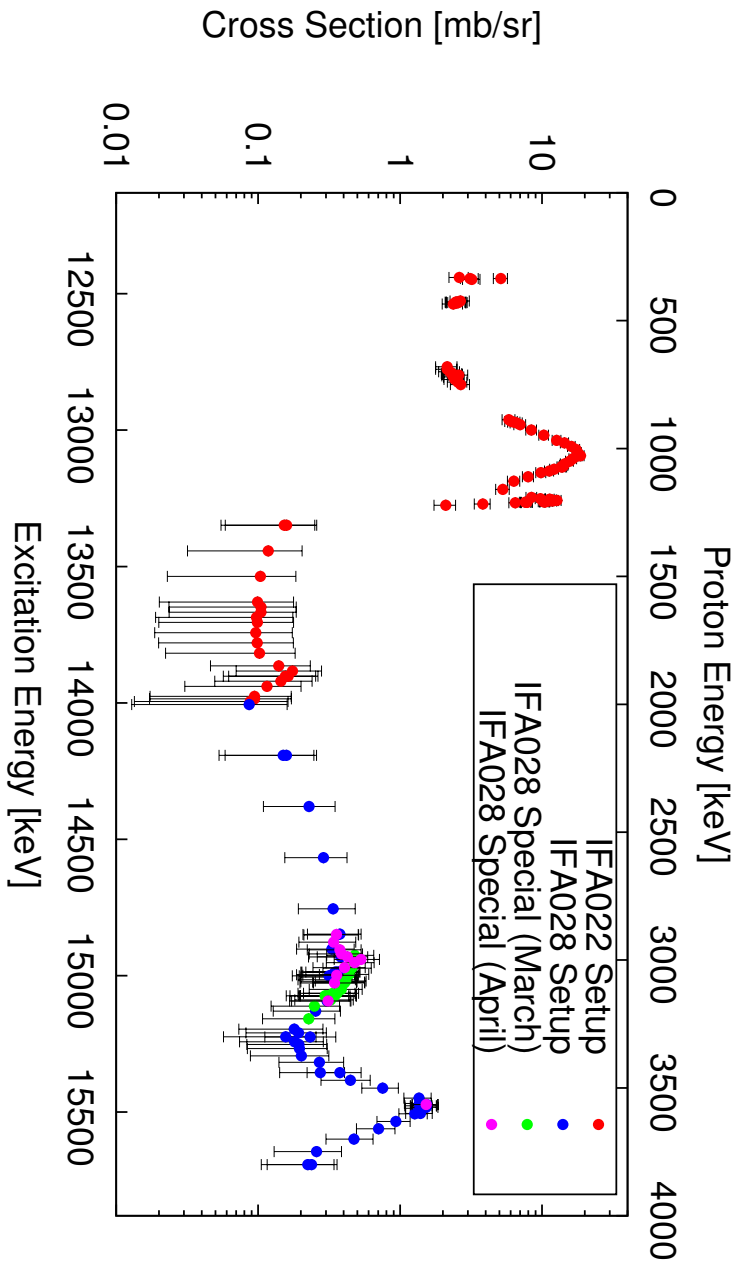

Figure 4: *Cross sections of the α_0 reaction as a function of energy.*

F - Full Energy Scan in α_1

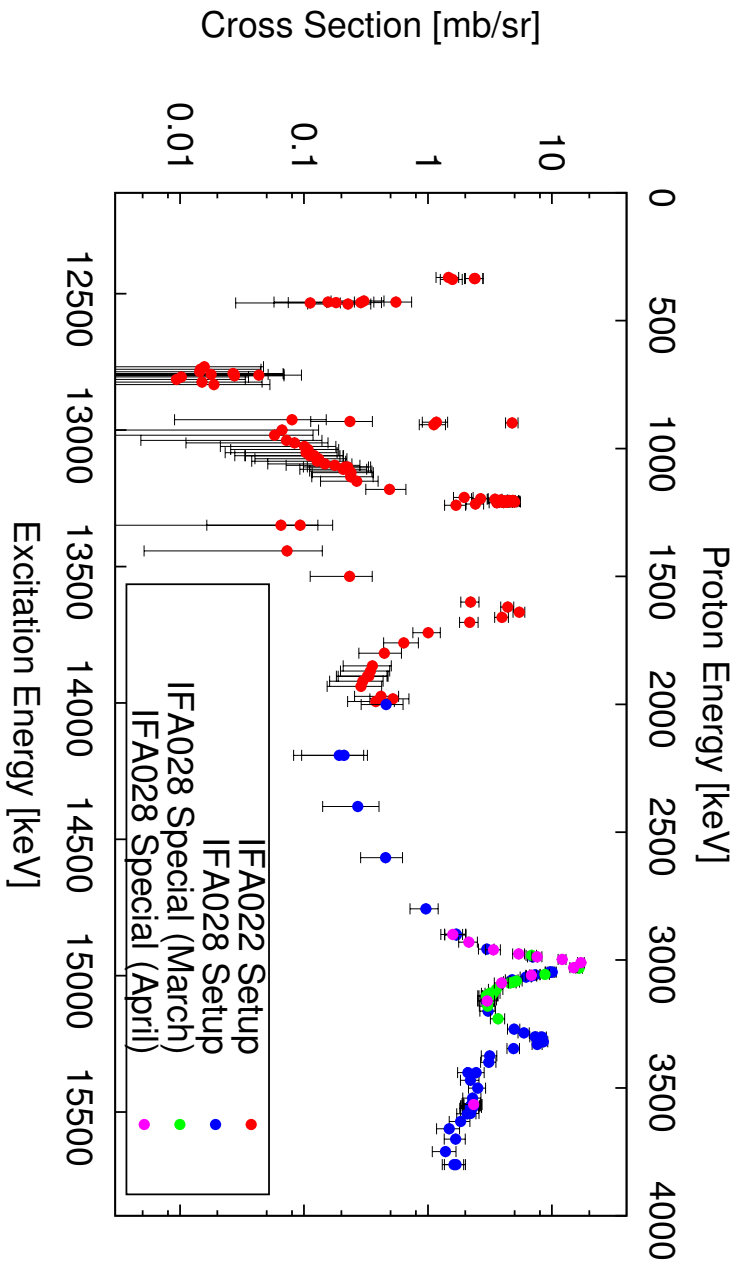

Figure 5: *Cross sections of the α_1 reaction as a function of energy.*